Detecting Electromagnetic Activity in Cerebral Organoids

Undergraduate Honors Thesis

By:

Reid Relatores

Advisor: Dr. Vish Subramaniam

Department of Mechanical and Aerospace Engineering

The Ohio State University

Autumn 2015

Abstract

The development of induced pluripotent stem cells (iPSC) has been an important stepping stone in research on the human brain. Any somatic cell can now be reprogrammed into an iPSC and coaxed into becoming neurons and other brain cells. Eventually, these cells can grow into structures resembling a developing human brain. These so called cerebral organoids have been allowed to mature to ~ 4 millimeters in diameter *in vitro* and show some signs of embryonic development. While it is possible to sustain these brain organoids for almost ten months, development appears halted at twelve weeks due to lack of a vascular system and other resource issues. Researchers at OSU hypothesize that by using electromagnetic fields maturation of these cerebral organoids can be accelerated and cellular differentiation can be influenced. Furthermore, if cerebral organoids exhibit some properties similar to the developing human brain, it is pertinent to explore whether or not there is any detectable electrical activity. The goal of this research is to develop a method to determine whether or not cerebral organoids exhibit electrical activity and whether there is any similarity to electrical activity in a developing human brain. Two methods are explored, one being a photoelectrochemical intrusive method wherein an electrode punctures the organoid while another rests in the media containing the organoid, and the other a non-contact electromagnetic method capable of detecting magnetic fields arising from neuronal currents. The results from the first photoelectrochemical method of detecting electrical activity is analyzed and investigated further. Ultimately, the aim of this research is to prove that electromagnetic activity is present in the organoid, and that it resembles similar activity in a developing human brain.

Acknowledgements

I would like to thank my advisor, Dr. Vish Subramaniam for his patience, mentorship and guidance, and his extensive knowledge on physics, chemistry, and biology.

I would like to thank Joe West for his technical assistance and all the help he provided me.

I would like to thank Dr. Rene Anand and Susan McKay for helping me understand biological concepts as well as providing the Applied Physics Lab with cererbral organoids.

I would like to thank Travis Jones and Josh Javor for the assistance they provided me when I began as well as an enjoyable lab environment.

Lastly, I would like to thank my parents, Menchu and Ranor, and brother, Reece for their love and support.

Table of Contents

List of Figures

List of Tables

List of Equations

Chapter 1

Introduction

1.1) *Background*

In 2006, a team led by Shinya Yamanaka successfully developed induced pluripotent stem cells (iPSC) from adult human somatic cells. These experiments have enabled many research investigations to be pursued without the need for a supply of human embryonic stem cells. Yamanaka would later win the Nobel Prize for this work in 2012. Only a year later, another team demonstrated complex cerebral organoids could be developed up to 12 weeks starting from iPSCs *in vitro* and could be preserved for up to 10 months [1]. By using different histopathological staining techniques they were able to show that physical structures normally observed in a 12 week old developing human brain were exhibited in the organoid.

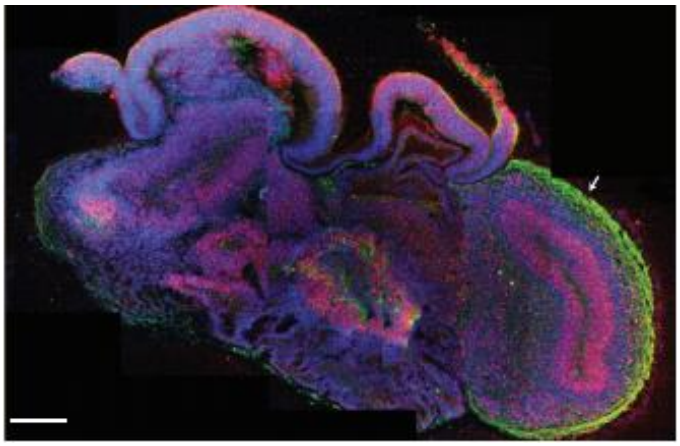

Figure 1: Fixed and stained organoid that shows complex morphology [1].

At OSU, Dr. Rene Anand's group in collaboration with the Applied Physics Laboratory has replicated this achievement and explored the use of weak electromagnetic fields in influencing organoid maturation. Cerebral organoids were subjected to weak induced electromagnetic (EM) fields similar to what has been previously used in experiments on electrotaxis and wound healing using redox based bioelectric dressings [2 -4]. When subjected to weak induced electric (E) fields with magnitude on the order of ~ 1 μV/cm over a period of 4 weeks, they found that the organoids exhibited maturity (as determined by gene expression and proteomics analysis) comparable to organoids that have not been subjected to E fields but allowed to develop for 12 weeks. While the reason for this acceleration in development is not understood and is being presently investigated, analysis of the expression (via measurement of messenger RNAs or mRNAs) of over 20,000 genes from organoids subjected to and not subjected to induced E fields has revealed that over 30 genes are up-regulated (increase in mRNAs) while over 30 other different genes are down-regulated (decrease in mRNAs). While the response of cerebral organoids to induced E fields is new, interesting, and may yield insight into the development of organoids, what is significant is that there is a response to EM fields in the first place. The next logical step in this research is to explore whether or not there is electrical activity in the maturing organoids.

1.2) *Motivation*

Cerebral organoids represent the next generation of stem-cell derived tools for understanding mechanisms of disease, stem cell therapies, tissue engineering, toxicological screens, as well as drug discovery. In the future, organoids will allow researchers to study a variety of neurological diseases in early stages of brain development. For example, organoids modeling autism could be used to screen potential drugs, *in vitro*, that could reverse synaptic

deficiencies in the brains of patients with autism. Another example that almost everyone has been directly or indirectly affected by is nicotine addiction. The human brain is one of the most affected tissues in tobacco use and can be used to address the toxicity of new tobacco products such as e-cigarettes and smokeless tobacco. Autism and nicotine addiction are only a few examples of organoid technology use in the future. From an engineering prospective, being able to study the brain *in vitro* could provide insight on how the human brain stores data. Increasing memory capacity and storage could make huge leaps in artificial intelligence, machine learning, new biological computers, and human-machine interfaces. By demonstrating that cerebral organoids exhibit electrical activity similar to developing human brains would verify their legitimacy as models for future neurological research as well as contribute to a better understanding of the human brain.

There are several methods that exist for detecting electric activity in the brain. Magnetencephalography (MEG) is sensitive enough to detect magnetic fields on the order of (10^{-18} T). Magnetic fields from synchronized groups of neurons are detected in real-time (millisecond time scale) from around a centimeter outside of the scalp [5]. MEG is extremely expensive and utilizes sensitive SQUID (Superconducting Quantum Interference Device) detectors that require cryogenic cooling and is therefore in the case of organoids, is an impractical method. Electroencephalography (EEG) is another electric measurement technique in which electrodes are placed on the scalp to detect any brain activity occurring over a defined period of time. For *in vitro* organoid experiments EEG requires electrodes to be inserted or to be in contact with the organoids. In this thesis, a measurement technique is described that is relatively inexpensive, sensitive enough to detect brain activity, and non-invasive so as to preserve the organoids for further analysis.

1.3) *Objectives*

Electromagnetic (EM) activity in intact cerebral organoids is explored for the first time, in this research. The first objective is to determine whether or not there is EM activity in organoids, and if this activity bears any resemblance to electrical activity in developing human embryonic brains. Two methods are developed in order to monitor EM activity from organoids. One technique is intrusive while the other is non-intrusive.

An electromagnetic coil is used as a probe to non-intrusively measure small magnetic inductions (B Fields). A dual coil probe comprising primary and detector coils will be investigated along with a single coil probe comprising only a detector coil. As a preliminary step to achieving this goal, an electronic circuit is developed that periodically produces the pulse resembling a neural action potential.

The second objective of this research is to use optical and chemical means to stimulate cerebral organoids, monitoring any EM activity that arises, and characterizing this activity. Any resulting EM activity is then compared to human brain EM activity.

Chapter 2

Electromagnetic Methods

2.1) *Experimental Simulation of a Neuronal Current and associated Magnetic Field*

To verify that an EM probe is capable of detecting the small magnetic fields associated with neuronal currents in the organoid an experimental simulation of a neuron is devised. The magnetic field from a single neuron carrying a propagating action potential and associated current is simulated experimentally using a current carrying wire of similar dimensions to a human axon. Although the magnitude of B fields around a single human axon due to action potentials is extremely small and negligible even to sensitive MEG devices [5], the crayfish axon B field is comparable to a human axon bundle (50,000 – 100,000) neurons and can be a basis for experimentally simulating neuronal currents.

2.1.1) *Neuron Physiology*

Electrical signaling in neurons results from ions flowing in and out of the axon. A neuron receives information at its dendrites via neurotransmitters resulting in sodium ions (Na+) flowing into and potassium ions (K^+) flowing out of the beginning (i.e. one end) of the axon [6].

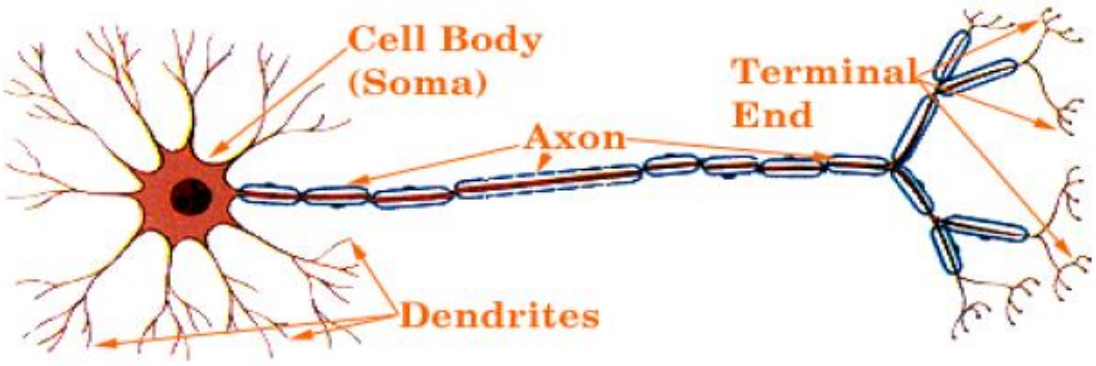

Figure 2: Neuron cell body [6]

This results in a potential difference between the inside and outside of axons, causing a change in the transmembrane potential, called an action potential, and triggers a chain reaction that propagates down the axon. Associated with a propagating action potential is an intracellular lateral neuronal current that produces a proportional magnetic field (B field) around the axon, by Ampere's law.

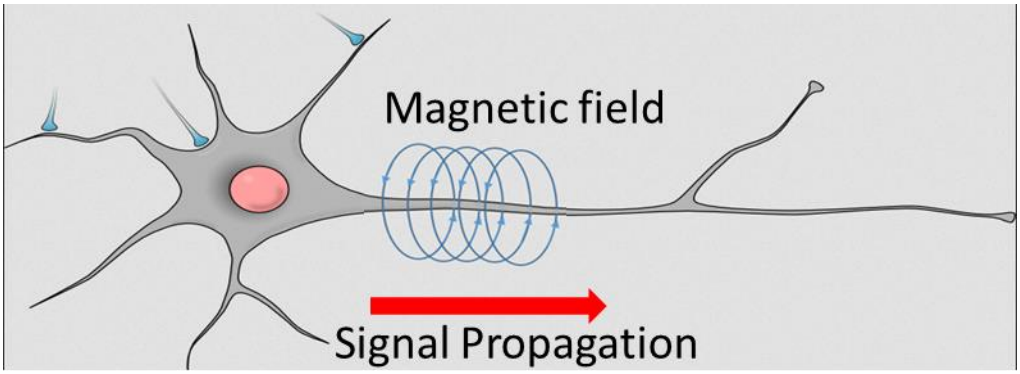

Figure 3: Magnetic field developing around axon due to propagation of action potential

$$Ampere's\ Law$$

$$\mu_o \vec{j} = \vec{\nabla} \times \vec{B} \qquad (1)$$

where $\mu_o$is the magnetic permeability of free space and $\vec{j}$ is the current density in the axon. Transmembrane and external lateral current contributions to the magnetic field around the axon are miniscule compared to the magnetic field produced by internal lateral current and are therefore negligible. The magnitude and waveform of an axonal B field has already been previously defined for a giant crayfish axon. [7].

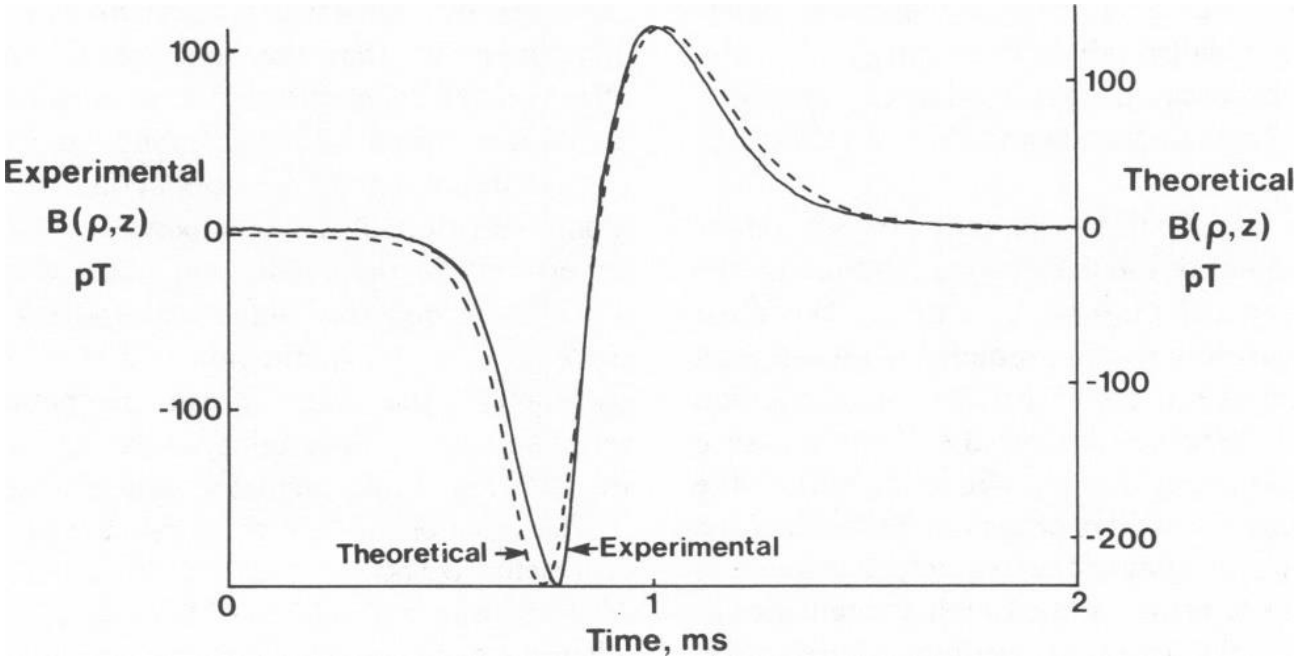

Figure 4: Experimental measurement and theoretical calculation of a giant axon of a crayfish (utilized SQUID sensors). A=.107 mm p =1. 48mm u=16.5 m/s

The depolarization and repolarization of the axon's membrane potential results in a waveform similar to an inverse sine wave with a frequency of 1000 Hz and a magnetic induction on the order of magnitude picoTeslas (pT).

2.1.2) *Replication of Axonal B Fields*

Intercellular neuronal currents (I) can be determined to be on the order of nanoAmperes (nA) in order to generate human axonal B fields on the order of picoTeslas (pT), using the Kelvin-Stokes theorem in conjunction with Ampere's law:

$$\int (\vec{\nabla} \times \vec{B}) \cdot d\vec{A} = \mu_o \int \vec{j} \cdot d\vec{A} \quad (2)$$

$$\oint \vec{B} \cdot d\vec{l} = \mu_o I \quad (3)$$

$$\frac{2\pi r B_{axon}}{\mu_o} = I \quad (4)$$

Similar axonal B fields can be generated then by applying a periodic voltage over a short segment of copper wire that is approximately the same diameter as a human axon (25μm) to simulate a propagating action potential.

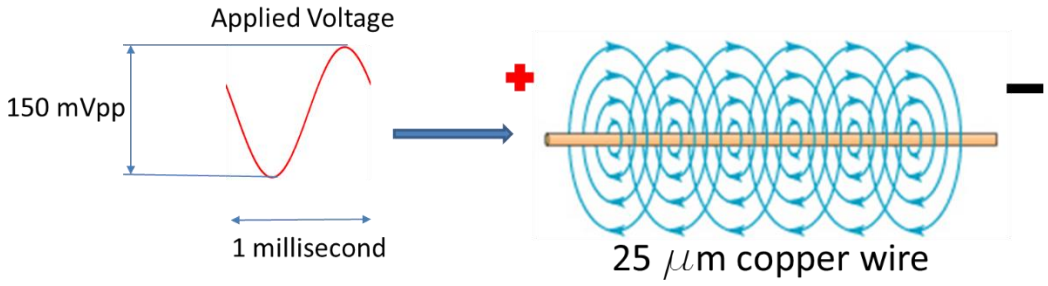

Figure 5: Experimental simulation of an axonal magnetic field

The simulated axonal magnetic field is generated using an Agilent 33220A function generator that outputs a 180 degree phase shifted sine wave with a 150 mV peak-peak voltage and a duty cycle of 1 kHz. A 500kW ballast resistor is used to generate a constant current of 300

nA. The function generator operates in burst mode which allows for outputting only one period of the sine wave at a fixed frequency. For modeling purposes, the neuron/axon can be represented by a simple resistor circuit, as shown in Fig.8.

2.2) *Electromagnetic Probe*

Previous work in the Applied Physics Laboratory have utilized a dual coil probe (but with very different coil characteristics) to measure tiny magnetic inductions (B fields) in freshly harvested tissue, to control migration of cells via electrotaxis, and for eddy current microscopy of tissue [2, 3, 8]. The dual coil system is comprised of an inner primary coil and an outer detector coil that is coaxially wound. By applying a time-varying voltage such as a sawtooth function (7Vpp and 100 kHz), a magnetic field is generated around the primary coil via Ampere's Law (1). An associated electric field develops by Faraday's Law in both the detector coil as well as in a sample placed nearby, causing currents to flow in both, which then results in associated magnetic fields.

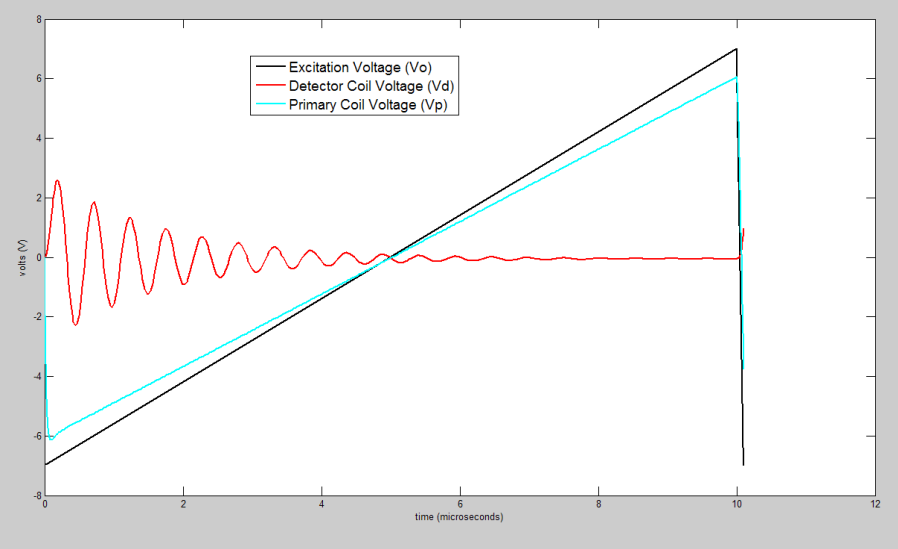

Figure 6: Voltage traces of the outputs of the primary and detector coil and the excitation voltage trace.

This interaction in which a voltage arises in the detector due to the coupled primary coil's magnetic field is termed mutual induction. When axonal magnetic fields are brought near the coils (<1mm), it affects this mutual induction which results in changes in the detector coil's voltage output. These changes include amplitude, time between peaks, and phase shifts that can be detected using lock-in amplification.

In order to optimize the EM probe, a circuit element model is developed for the case where neuronal magnetic fields are absent as well as when neuronal magnetic fields are present. In each case the governing systems are derived. The detector coil contains wire resistance (R_d) that accounts for the resistivity of the wire, an in series self-inductance (L_d), and a parallel lumped capacitance (C_d) that accounts for the capacitance between wire windings and capacitance between layers of windings. In a similar manner, the primary coil parameters are R_p, L_p, C_p, and an additional ballast resistance R_b. As previously stated, the two coaxial wound coils

are mutually coupled and therefor is represented by M_{pd} and M_{dp}. When an axon is present, a mutual induction between the axon and primary coil exists (M_{ap}) as well as a mutual induction between the axon and the detector coil (M_{ad}). The voltage applied across the primary coil and experimental simulation of a neuron is represented by V_o and V_a, respectively. The output voltage across the primary coil and detector are V_p and V_d, respectively.

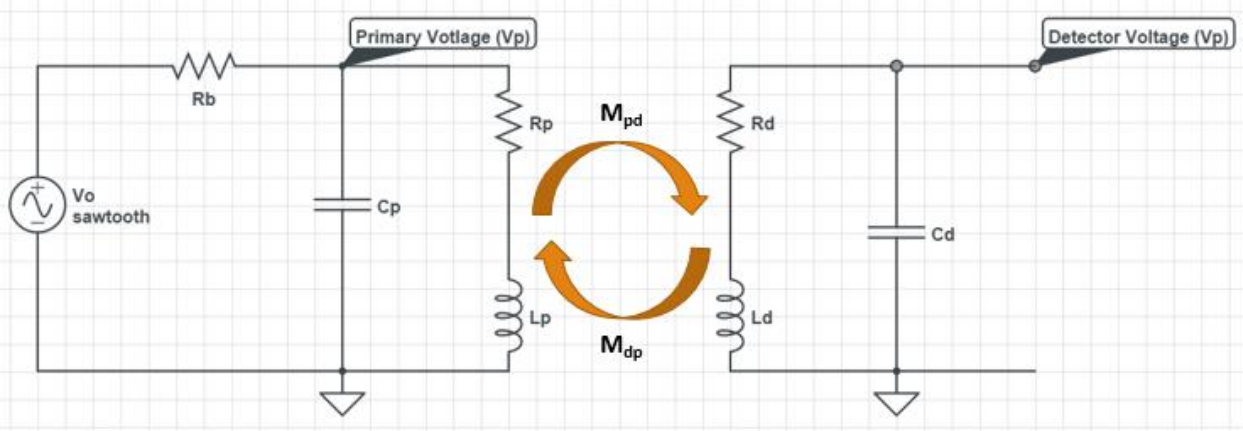

Figure 7: Circuit diagram of electromagnetic probe without experimental simulation of the neuron

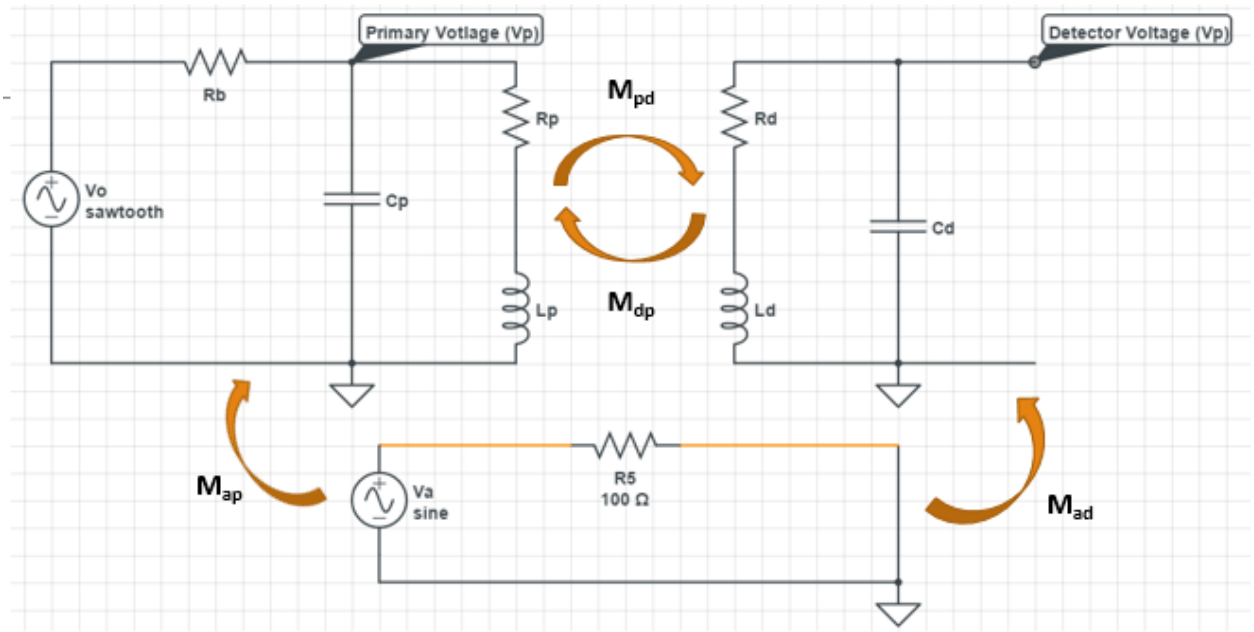

Figure 8: Model of electromagnetic probe with experimental simulation of the neuron

Using this simplified EM probe circuit and Kirchhoff's voltage and current laws the governing equations can be derived. In the case where an axon is in proximity of the EM probe, the mutual inductance between the axon and the coils (M_{ap}, and M_{ad}) are present in the equations. When the axon is absent, these mutual inductances simply go to zero and drop out of the equations.

Primary Coil Equations:

$$C_p \frac{dV_p}{dt} = \left[\left(\frac{V_o - V_p}{R_b}\right) - i_p\right] \quad (5)$$

$$M_{ap}\left(\frac{di_a}{dt}\right) + L_p \frac{di_p}{dt} + M_{pd}\left(\frac{di_d}{dt}\right) = \left[V_p - R_p(i_p)\right] \quad (6)$$

Detector Coil Equations:

$$\frac{dV_d}{dt} = \frac{i_d}{C_d} \quad (7)$$

$$M_{ad}\left(\frac{di_a}{dt}\right) + L_d\frac{di_d}{dt} + M_{dp}(\frac{di_p}{dt}) = -V_d - R_d(i_d) \quad (8)$$

To make it possible for the probe to be able to detect the presence of the axon, the values of each term in differential equations (5) to (8) must be around the same order of magnitude. Previous work has shown that it possible to analytically approximate a coil's resistance (R), self-inductance (L), and mutual induction between coils (M) if the coil characteristics are known [8, 14] i.e. wire gauge, wire material, windings per layer, inner coil diameter, outer diameter, and the number of coil layers . To confirm the resistance and induction calculations measurements are taken using an LCR meter. The coils' lumped capacitance (C) cannot be calculated or measured at the higher frequencies. Consequently, it must be inferred at lower frequencies (~ 1 kHz) by comparing model and experimentally measured detector voltage waveform.

Since the axon's magnetic field is a fixed (i.e. known) quantity and represented by the axon-coil mutual inductances multiplied by the derivative of the current through the axon, manipulation of coil parameters is the only viable option. Before optimizing the coil's resistance, inductance, and capacitance, the axon-coil mutual inductance must be determined.

The mutual inductance between a straight current carrying wire and a single loop of wire is used as the basis for analytically calculating the mutual inductance between the axon and EM probe. Where ***s*** is the radial distance the loop of wire is from the straight wire, ***r*** is the radius of the loop of wire, and $\mathbf{X_c}$ and $\mathbf{Z_c}$ denote center distances with respect to their axis.

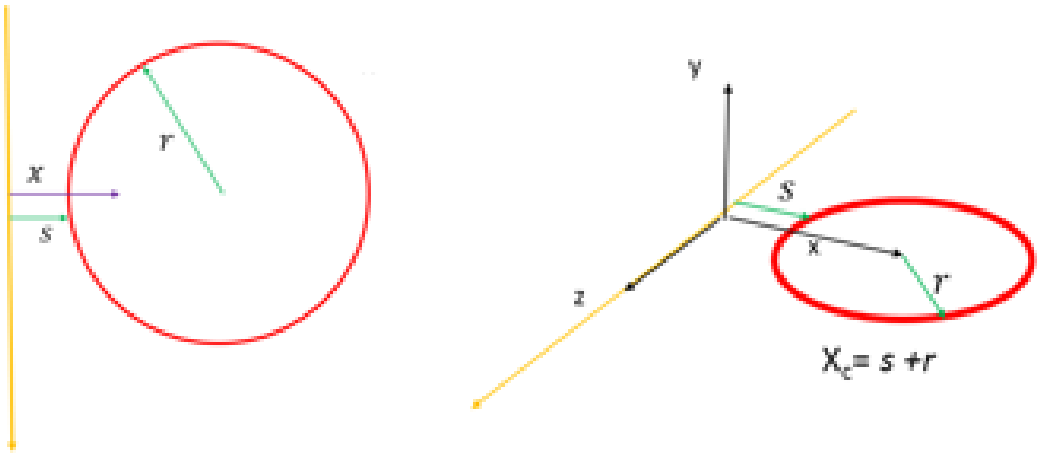

a) **b)**

Figure 9: 2D a) and 3D b) view of the straight current carrying wire (yellow) and circular loop of wire (red)

To determine the mutual inductance, it is necessary to calculate the magnetic flux through the circular loop. Using Ampere's Law, the total magnetic flux can be found by integrating the B field over the cross sectional area of the circular loop.

$$B_{axon} = \frac{\mu_o I_a}{2\pi r} = \frac{\mu_o I_a}{2\pi\sqrt{x^2 + y^2}} \quad \textbf{(9)}$$

$$\Phi_B = \int d\Phi_B = \int \vec{B}_{axon} \cdot d\vec{A} = \int B_{axon} A \cos\theta \quad \textbf{(10)}$$

$$\cos\theta = \frac{x}{\sqrt{x^2 + y^2}} \quad dA = dzdx \quad \textbf{(11)}$$

$$\Phi_B = \iint \left[\frac{\mu_o I_a}{2\pi\sqrt{x^2 + y^2}}\right]\left[\frac{x}{\sqrt{x^2 + y^2}}\right] dzdx \quad \textbf{(12)}$$

The limits of integration are determined by the location of the loop with respect to the origin. For the case in Fig. 9 the limits of equation are as follows:

$$\Phi_B = \int_{Xc-r}^{Xc+r} \int_{Zc-r}^{Zc+r} \left[\frac{\mu_o I_a}{2\pi\sqrt{x^2+y^2}}\right]\left[\frac{x}{\sqrt{x^2+y^2}}\right] dz\, dx \quad \textbf{(13)}$$

Thus, the mutual induction between a single loop of wire and a straight current carrying wire can be calculated by simply dividing the magnetic flux by the current through the straight wire.

$$M_{single} = \frac{\Phi_B}{I} = \int_{Xc-r}^{Xc+r} \int_{Zc-r}^{Zc+r} \left[\frac{\mu_o x}{2\pi(x^2+y^2)}\right] dz\, dx \quad \textbf{(14)}$$

The mutual inductance between a single wire and a straight wire can be applied to an EM probe that could consist of multiple layers and multiple windings.

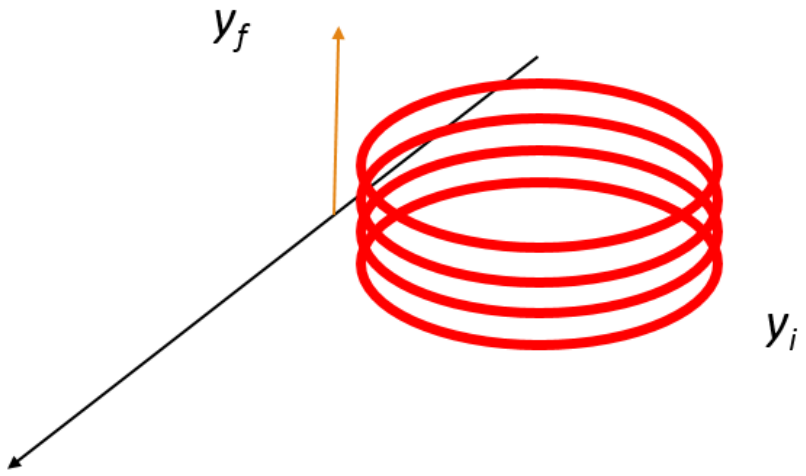

Figure 10: Multiple loops of wire next to current carrying wire

Each winding in the coil corresponds to a different height (y_i), where y_o represents the height of the bottom loop in the coil and y_f corresponds to the top loop of wire in the coil. Equation **(**15)

below is used to find the mutual inductance at each height. Once all the individual mutual inductances are found at each height, they are all summed together to find the mutual inductance (M_{layer}) between one layer of the coil and the axon.

$$M_{layer} = \sum_{yo}^{yf} \int_{Xc-r}^{Xc+r} \int_{Zc-r}^{Zc+r} \left[\frac{\mu_o x}{2\pi\left(x^2 + y_i^{\,2}\right)}\right] dz\, dx \quad \textbf{(15)}$$

To account for multiple layers and approximate the total mutual inductance (M), M_{layer} is multiplied by the number of layers in the coil.

$$M = K \sum_{yo}^{yf} \int_{Xc-r}^{Xc+r} \int_{Zc-r}^{Zc+r} \left[\frac{\mu_o x}{2\pi\left(x^2 + y_i^{\,2}\right)}\right] dz\, dx \quad \textbf{(16)}$$

Chapter 3

Experimental Measurements on Cerebral Organoids

The EM probe is still being developed and was not available at the time of writing of this thesis so intrusive wire probe methods were used to detect electrical activity from cerebral organoids. The experiment was conducted on a 15 week old organoid that had been exposed to small electromagnetic fields (~ μV/cm) during its development. When illuminated with a 532nm green laser a small retinal cup became visible on the organoid (Fig. 11)**.**

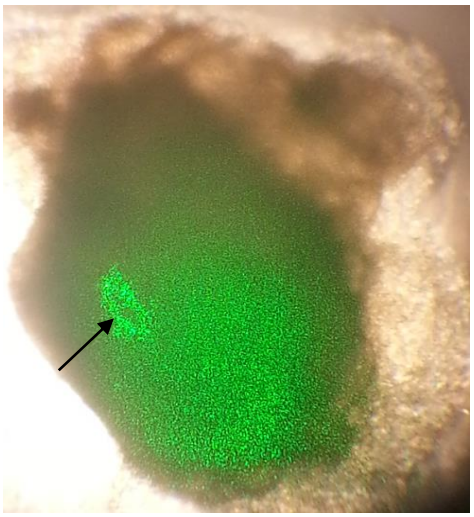

Figure 11: Organoid with retinal cup indicated with black arrow

3.1) *Experimental Setup*

A glass slide with a custom made well was used to hold the organoid. The organoid is immersed in a solution consisting of a combination of 150 μL of GIBCO® HBSS and 15μL of 100mM glutamic acid. HBSS is a salt solution that provides nutrients in which the organoid is

grown and maintained. Glutamic acid (glutamate) is a well-known excitatory neurotransmitter seen in the human brain. To detect any change in potential a 30 AWG Au wire is inserted in the media and serves as electrical ground while the other 31 AWG burnt copper wire electrode punctures the organoid (Fig. 12)

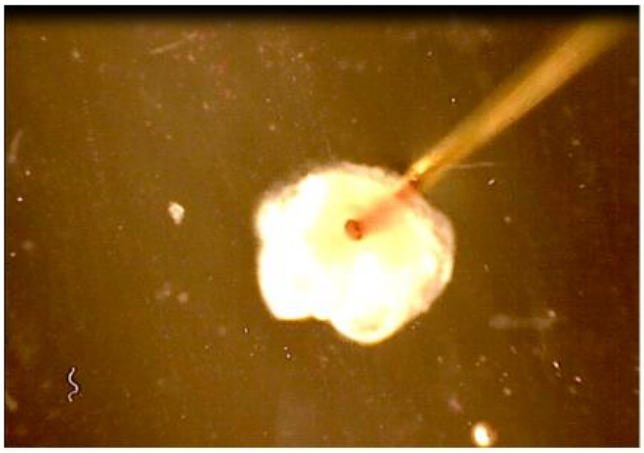

Figure 12: Organoid pierced with burnt copper wire electrode

An Agilent DS0-X 2014A oscilloscope was used to continuously monitor the voltage output. To stimulate the organoid optically, a 532 nm 14.6mW green laser was used to trigger an electrical response from the organoid. Glutamate blockers (10 μM of CNQX and AP5) are used to counteract the effects of the glutamate by blocking any glutamate receptor sites on the neurons of the cerebral organoid and therefore suppressing the signal.

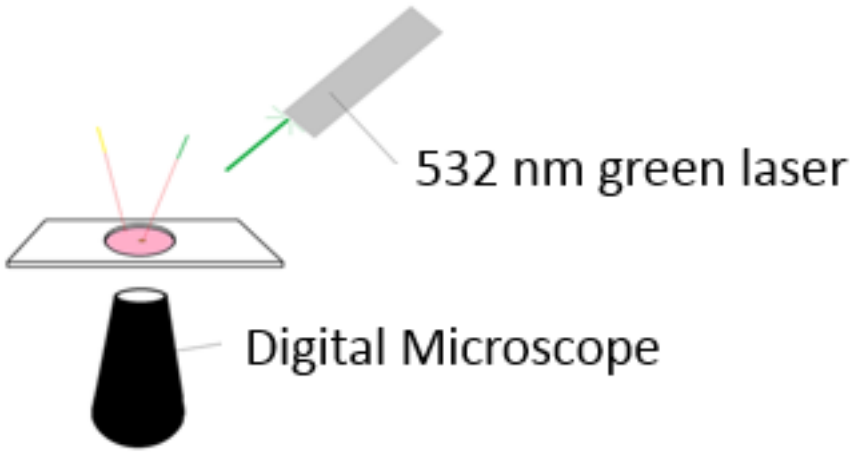

Figure 13: Diagram of green laser and digital microscope

3.2) *Experimental Results*

Figure 14 shows the voltage difference between the two wires (gold and burnt copper inserted in the organoid) over a two and a half minute period. As the organoid rests in 150 µL HBSS and 15 µL glutamate (indicated by "1") there is a 2mV resting potential with no significant change in voltage. At the instant marked as "2", the laser light is incident on the organoid there is a choppy transient voltage response. Note that there appears to be two voltage rises. The first voltage rise appears from around 12 seconds to 35 seconds and the second from 35 to 88 seconds. The laser is then blocked at "3" which results in a drop in voltage. The laser is then unblocked at "4" and the voltage quickly rises to the original level. After glutamate blockers are added, with the laser light still on, the signal drops to down to 4mV. It is important to note that the final potential is approximately 2mV greater than the starting potential. This will be explained in greater detail in Chapters 4 and 5.

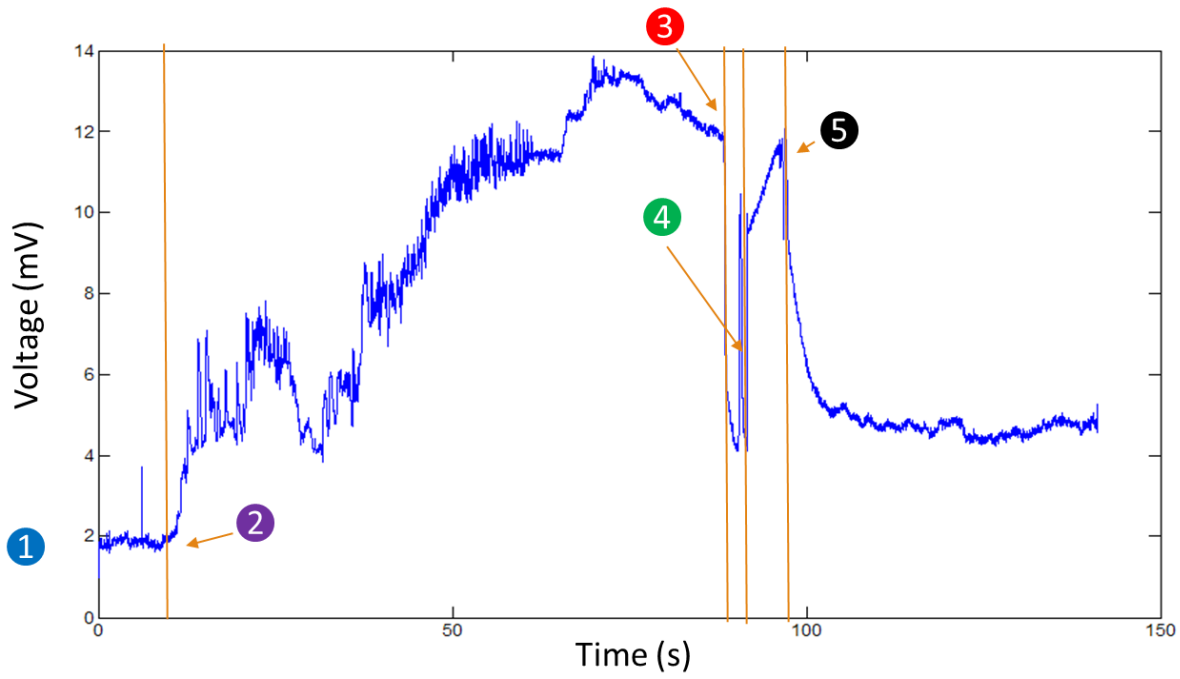

Figure 14: Voltage trace of organoid experiment with indicators

It can be seen from Fig. 15 that in certain portions of the voltage signal obtained from the cerebral organoid, that there are oscillatory signals present. These are depicted in color in Fig. 14, which is the same data as in Fig. 15. The colored portions of the signal have been extracted, rendered periodic by repeating that portion of the signal 10 times so that a Fast Fourier Transform (FFT) analysis can be performed [15]. The MATLAB script used to generate the FFT can be seen in Appendix B. The results from the FFT analysis of the data shown in Fig. 14 and 15 are shown in Figs. 16-20. It can be seen that periodic oscillations of several frequencies exist. The most discernible frequencies occur in the initial rise from approximately 10-35 seconds and are analyzed in Figs. 16 and 17. Figure 16 shows the FFT of phase one that occurs from 12 to 21 seconds and Figure 17 shows the FFT of the signal from 21 to 27 seconds. It can be seen that there may be frequencies below 11 Hz that are present. The next rise in voltage is analyzed in

Figs. 18 and 19. Figures 18 and 19 show the FFT of the portion of the signal from 53 to 59 seconds and from 59 to 65 seconds, respectively. In these portions, the presence frequencies around 1 Hz, 2 Hz, 4 Hz, and 5 Hz are very apparent. Lastly, the FFT of the portion of the signal in Figs. 14 and 15 in which almost no frequencies are apparent, is shown in Fig. 20. The FFT of the signal ranges from 73 to 80 seconds. It can be seen that the frequencies that were present in Figs. 16-20 disappear and their corresponding amplitudes are virtually zero.

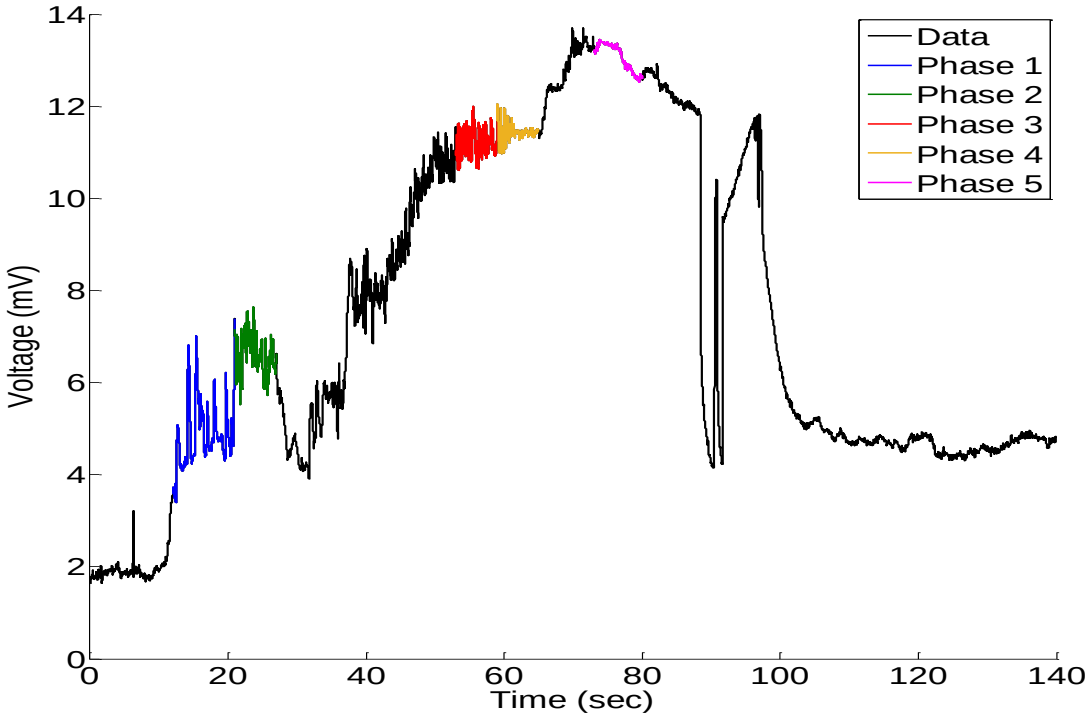

Figure 15: Voltage trace of organoid experiment showing phases 1-5

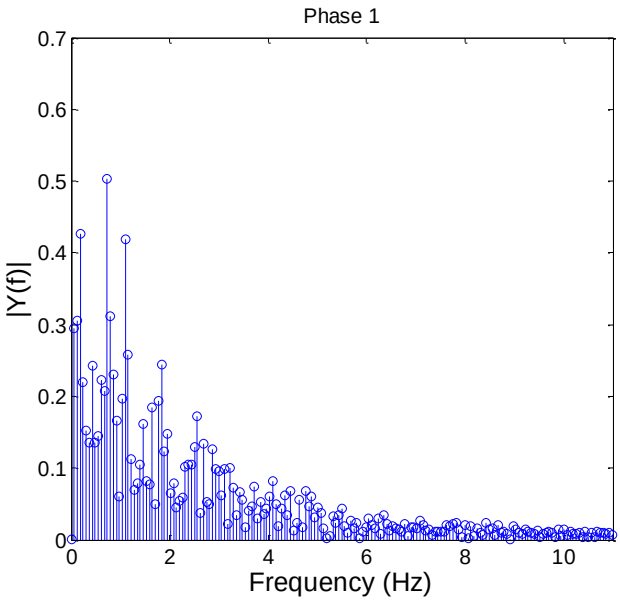

Figure 16: Fast Fourier Transform of the portion of the signal shown in Figs. 14 and 15, from 12 to 21 seconds.

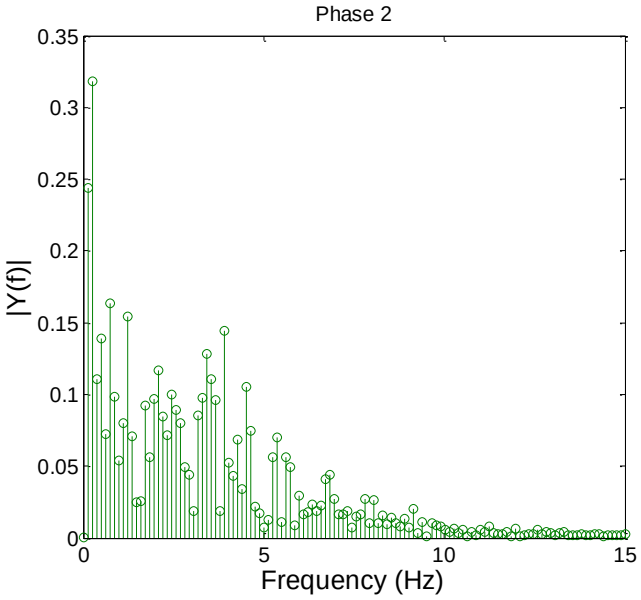

Figure 17: Fast Fourier Transform of the portion of the signal shown in Figs. 14 and 15, from 21 to 27 seconds.

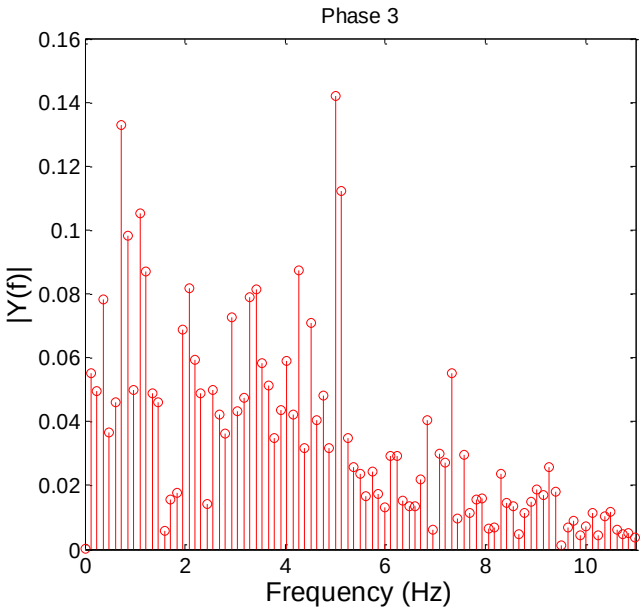

Figure 18: Fast Fourier Transform of the portion of the signal shown in Figs. 14 and 15, from 53 to 59 seconds.

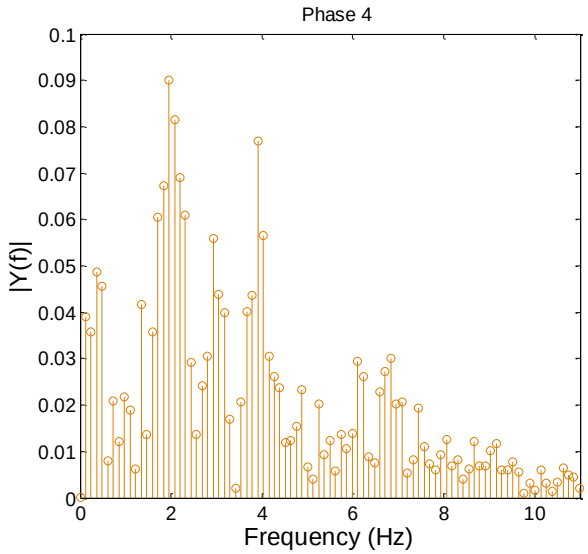

Figure 19: Fast Fourier Transform of the portion of the signal shown in Figs. 14 and 15, from 59 to 65 seconds.

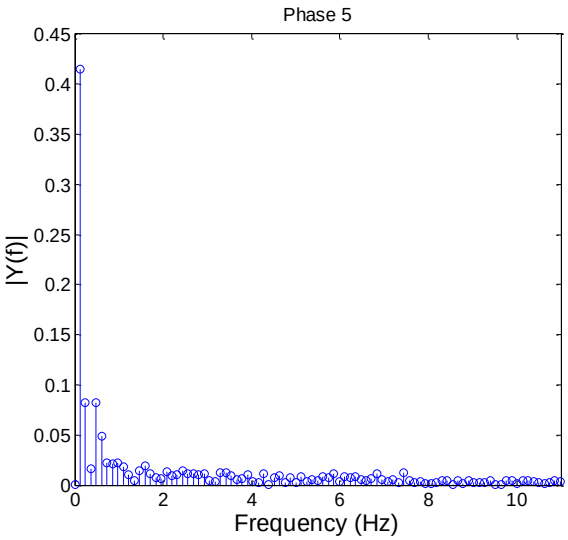

Figure 20: Fast Fourier Transform of the portion of the signal shown in Figs. 14 and 15, from 73 to 80 seconds.

3.3) *Significance of Fast Fourier Transform Analysis of Electrical Signal from Cerebral Organoid*

In the human brain there are a variety of different brain waves that are present during different activities. Table 1 lists some of these common brain waves and the frequencies at which they occur. Delta waves are common in deep dreamless sleep. Theta waves occur in a light sleep or times of extreme relaxation. Alpha waves are present when awake but not processing much information and beta waves occur when someone is wide awake [9].

Brain Wave	Frequencies
Delta	.5 – 3 Hz
Theta	3 – 8 Hz
Alpha	8 – 12 Hz
Beta	12 – 38 Hz

Table 1: Frequencies typically observed in human brains

From the results of the FFT analysis shown in Figs. 16-20, the major frequencies that appear to be present in the electrical signal obtained from the cerebral organoid are approximately 1 Hz, 2 Hz, 4 Hz, and 5 Hz which would correspond to delta and theta waves. It is possible that the observed frequencies could be harmonics from commonly observable 60 Hz noise random electrical noise. However, this is unlikely since the amplitudes in the FFT at these frequencies vanished when the glutamate blockers were added (Figs. 14, 15, and 20). This can only be explained by the fact that biological effects (i.e. addition of glutamate blockers) caused the observed peaks at 1 Hz, 2 Hz, 4 Hz, and 5 Hz to disappear.

Chapter 4

The Photoelectrochemical Phenomenon

It is pertinent to question the source of the electrical signal observed from the cerebral organoid and shown in Figs. 14 and 15. In the experiments on cerebral organoids, a 30 AWG 18 karat gold wire was used as the grounded (V=0) electrode and placed in the media in which the organoid was immersed. The positive (V) 31 AWG copper wire that had been previously burnt to remove its insulation was used as the electrode to puncture the organoid, while it was illuminated by visible radiation from a 532nm 14.3 mW green laser beam, as shown in Fig. 21.

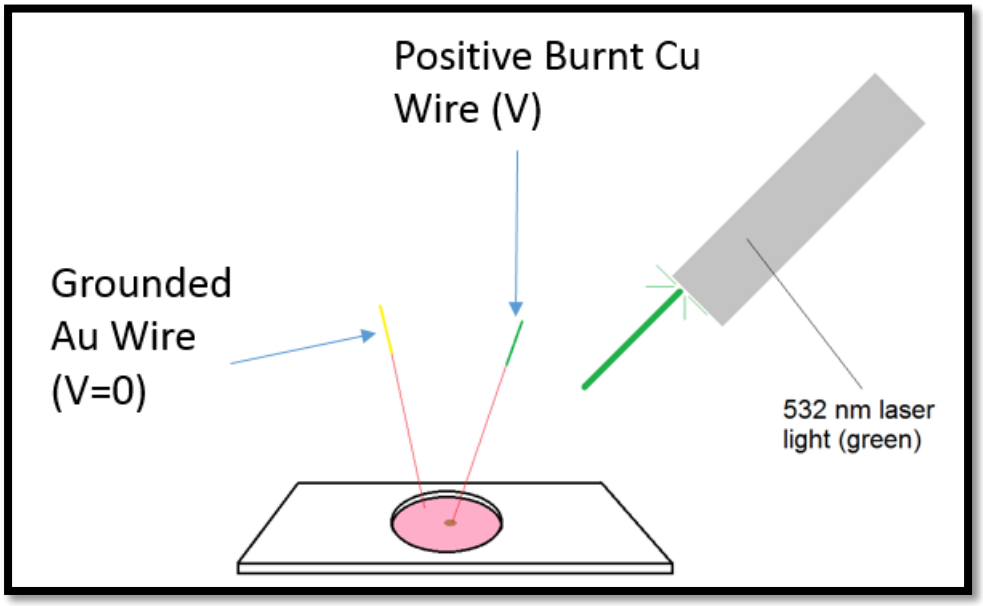

Figure 21: Experimental apparatus used to detect electrical activity in cerebral organoids using wire probes

To understand the underlying phenomenon that produced the electrical signal shown in Figs. 14 and 15, control experiments were conducted that isolated and or highlighted the importance of specific variables in the organoid experiments. These variables include laser wavelength and power, wire electrode material, pH of the solution in which the organoid was immersed, and the distance between the wire electrodes. During these control experiments, we uncovered a new phenomenon related to the earlier work of Edmond Becquerel which has been wrongly attributed to the photovoltaic effect. Although Edmond Becquerel has been given credit for discovering a method of converting light to electricity and giving birth to the field of photovoltaic conversion, his original experiments in 1839 involved light and electrolytes and is more aptly termed as a photogalvanic effect rather than a photoelectric effect. In this work, it will be shown that the electrical signal observed from the cerebral organoid is based on a photoelectrochemical effect, requiring the simultaneous presence of light, a p-type semiconductor, and aqueous electrolyte with the light incident at the junction between the semiconductor and the electrolyte.

4.1) *The Becquerel Effect*

In 1839, Edmond Becquerel discovered that by immersing two metal electrodes (with one being covering in a substance sensitive to light) in an acidic solution and illuminating one of the electrodes with light, an electric current is produced between them. He used a variety of metal electrodes including gold, brass, and platinum and used different silver halogen powder to coat one of the electrodes [10].

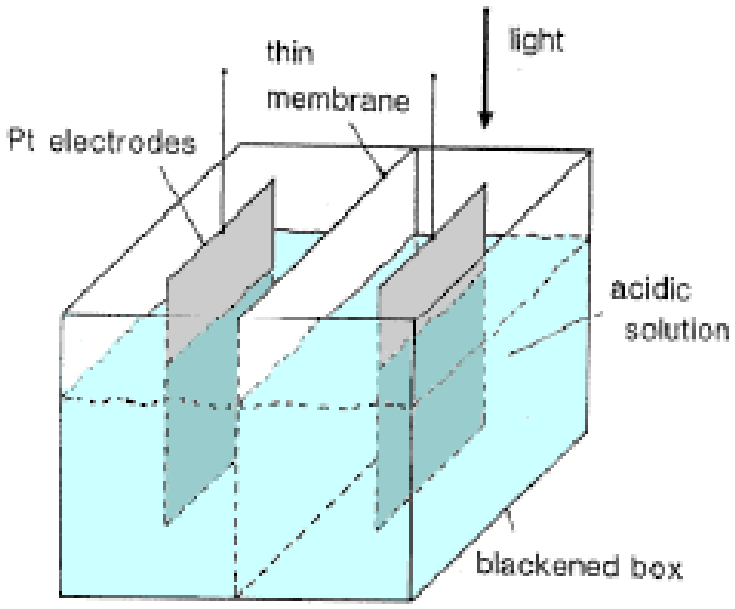

Figure 22: Experimental setup used by Edmond Becquerel in 1839 [10]

Becquerel reported that the largest currents were generated in acidic solutions and that the blue-violet spectrum of light is effective while the red is not [11]. For these experiments Becquerel is now acknowledged as the discoverer of the first photogalvanic cell and the photovoltaic effects. In the first half of the control experiments described in this chapter, an experimental setup similar to Becquerel's experiments is used in which the light sensitive electrode is part of the circuit and similar effects are observed. In the latter half of the chapter, a new setup in which the light sensitive electrode is not part of the circuit is described and results are presented.

4.2) *Experimental Setup*

The experimental apparatus used to interpret the electrical signal observed from the cerebral organoid is shown in Figures 23 and 24**.** A green 532 nm (14.3 mW laser) and red 632 nm (1.2 mW) laser are used to illuminate the cupric oxide samples. The laser power is measured

with the Scientech Vector S310 Power Meter with the AC2501 Power Meter head. The diameter of the green and red laser spots are approximately 1.5 mm and 3.25 mm, respectively. The spot size is measured by orthogonally irradiating a flat surface and measuring the diameter with a ruler. The laser is directed through a series of mirrors that can be adjusted with micrometer dials indicated in green in Figure 23. An MC1F2 optical chopper is used to chop the laser and serves as a reference for the lock-in amplifier. The reference or chopper frequency is 3 Hz for all control experiments.

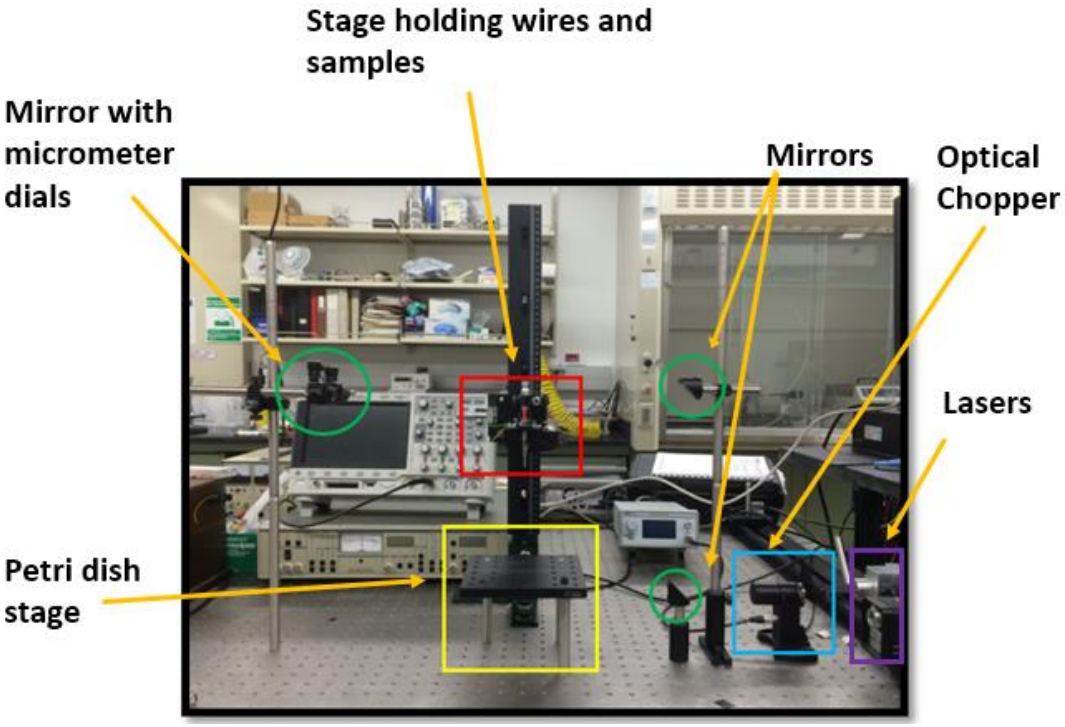

Figure 23: Photograph of experimental setup used in the photoelectrochemical effect experiments

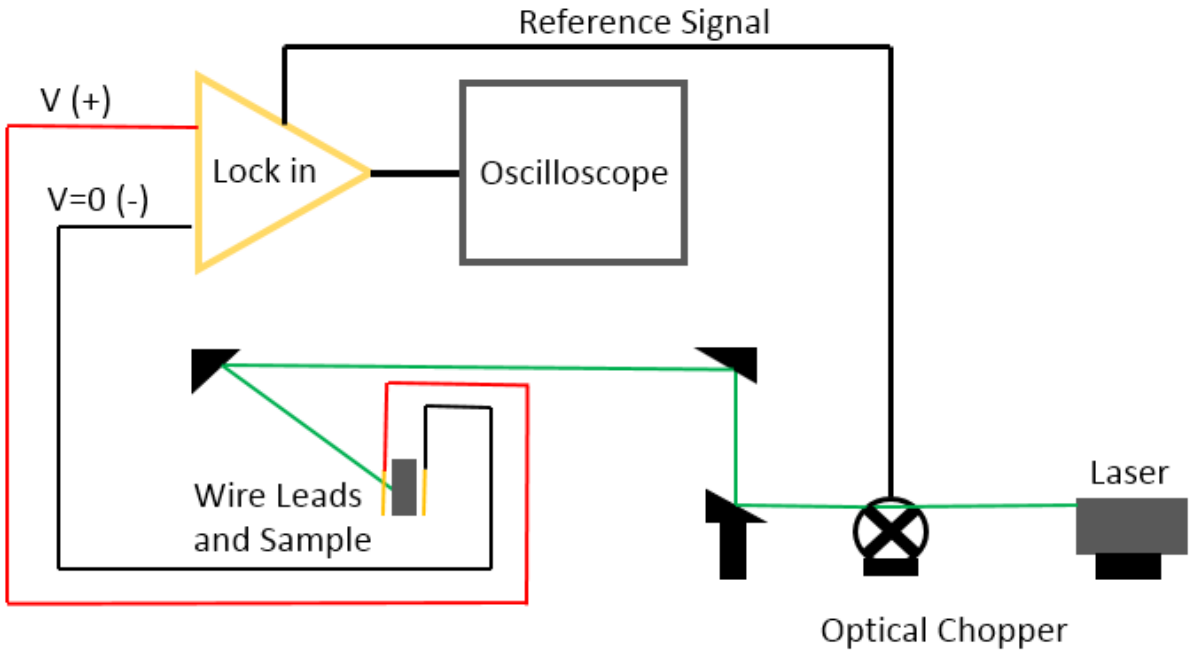

Figure 24: Diagram of experimental setup used in the photoelectrochemical effect experiments

The 30 AWG Au wire leads and cupric oxide (CuO) samples are attached to a stage (indicated in red) that can move vertically (z axis) as well as side to side (x axis). One wire lead is attached to a y axis micrometer while the other wire lead and sample are rigidly attached to the stage. Each wire is contained within a capillary tube to prevent any movement.

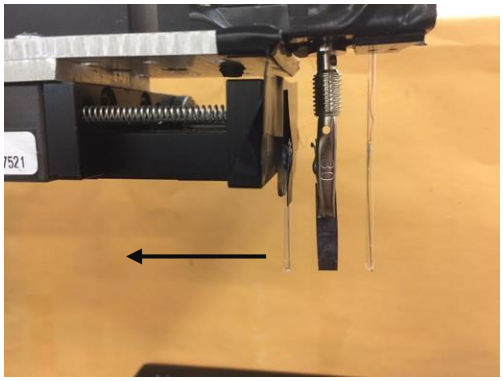

Figure 25: Stage holding sample and wire leads in capillary tubes

The output of the wire probes is connected to a Stanford Research System SR510 Lock-in Amplifier which is used to accurately detect small signals. By using the signal from the optical chopper as a reference, the amplifier is capable of locking in on the phase of the input signal which in turn eliminates random electrical noise. The DC voltage output from the lock-in amplifier is then sent to an Agilent DS0-X 2014A Oscilloscope for recording the data.

The SR510 Lock-Amplifier is able to detect changes in both magnitude and phase of the input signal and outputs the V_{DC} to the oscilloscope. Equation (17) shows the relationship between the lock-in settings and the V_{rms} of the input signal.

$$V_{DC} = 10A_e(A_v V_{rms} cos\emptyset + V_{os}) \quad \textbf{(17)}$$

where: A_e = 1 or 10 per the Expand setting, A_v = 1/Sensitivity, $V_{rms} = V_i/\sqrt{2}$, (for square wave), V_i = magnitude of signal, Ø = phase between signal and reference, and V_{os} = offset (not used).

Table 2 shows the lock-in amplifier settings used in all experiments except for the Ranging pH experiments. In the ranging pH experiments the lock in sensitivity used was 1mV/V and dynamic reserve is set to low but the rest of the settings are the same. The conversion of lock-in amplifier voltage outputs to actual voltages was done through MATLAB (Appendix C) and all plots display the actual voltages (V_i) of the signal instead of the lock in output (V_{DC}).

Lock in Setting	
Sensitivity (k)	20 mV/V
Pre time constant (τ_{pre})	1s
Post time constant	.1s
Dynamic Reserve	Normal
Expand	1

Table 2: Lock-in amplifier settings used in experiments

To replicate the burnt copper wire in the organoid experiments, pure 99.999 % .25 mm thick Puratronic copper foil purchased from Alfa Aesar is burned for 7-10 seconds with a Worthington propane torch to produce an outer layer of cupric oxide.

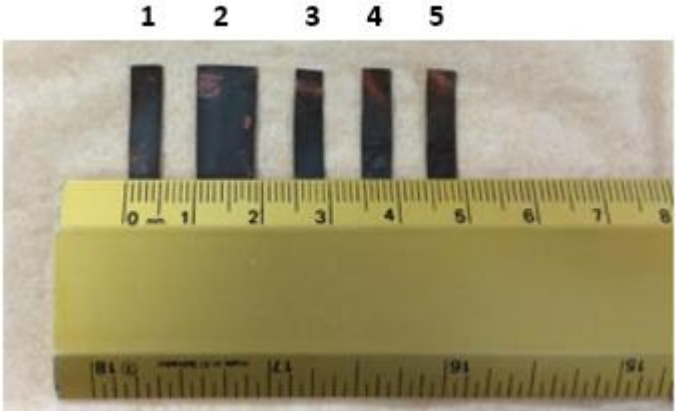

Figure 26: Cupric Oxide (CuO) samples used in the experiments

4.3) *Cupric Oxide Part of Circuit*

In the organoid experiments, the burnt copper wire punctured the organoid. This is replicated by having the cupric oxide foil as part of the circuit and illuminated with either green or red laser light. Figure 27 shows a detailed schematic of the experiment.

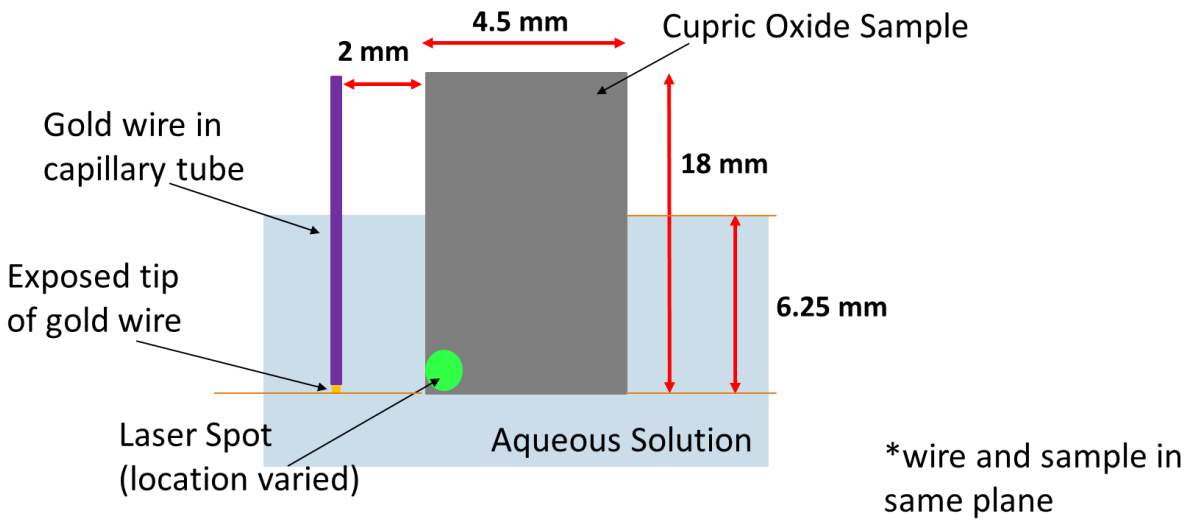

Figure 27: Diagram of gold wire and sample where CuO sample is part of the circuit

4.3.1) Deionized Water

Figure 28 shows continuous traces of the voltage obtained between the gold wire (positive, V) and the grounded CuO foil (V=0) for the case where the CuO foil is irradiated with the unfocused green laser in deionized water. The deionized water has a pH of 7.4 and a resistivity of 18.1 MΩ-cm and was obtained from a Direct-Q 3 Water Purification System.

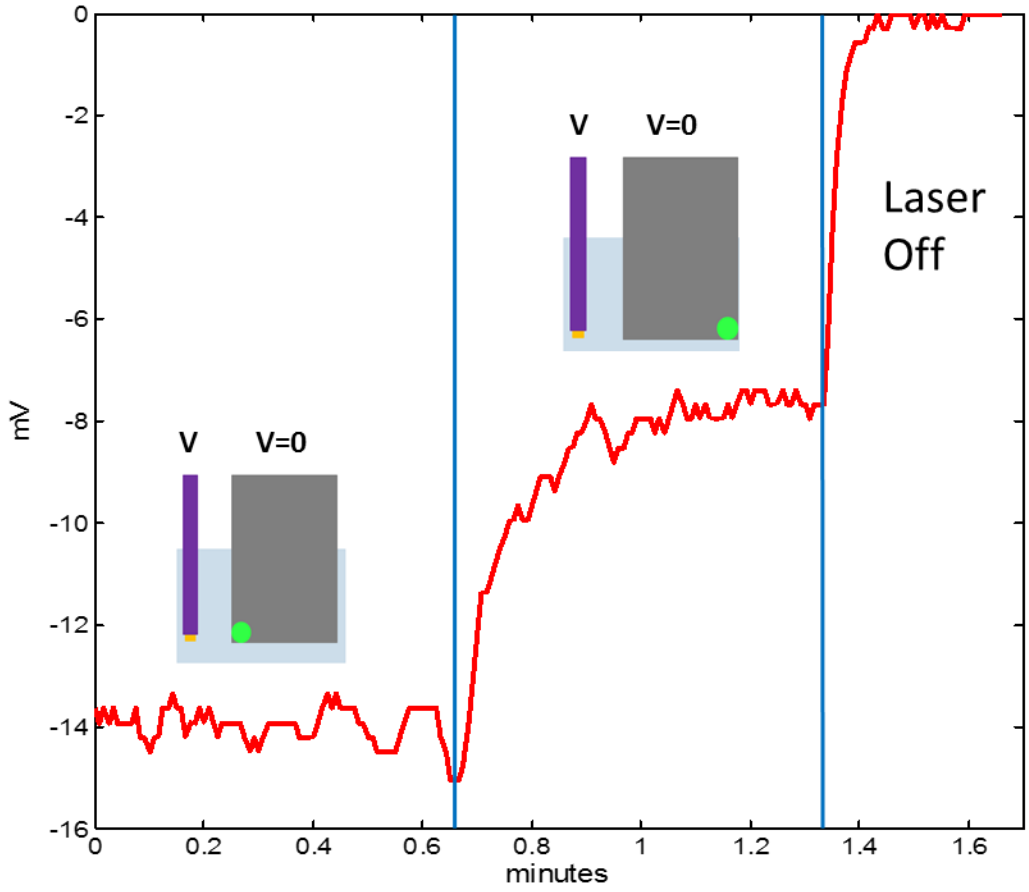

Figure 28: Voltage trace when using the green laser, deionized water, and the polarity of Au is (V) and the polarity of CuO is (V=0)

The laser first irradiates the sample in the lower left corner closest to the exposed gold wire tip and produces a -14 mV voltage. When the laser spot is moved farther from the exposed gold wire tip towards the lower right corner of the sample, the voltage drops to -8mV. Once the laser is shut off, the voltage output drops to zero.

Figure 29 shows the voltage trace when the polarities of the leads are switched. The voltage output is now positive. It is also important to note that similar effects to those shown in

Fig. 28 are observed here, where the distance from laser spot to exposed gold wire tip dictates the magnitude of the voltage output.

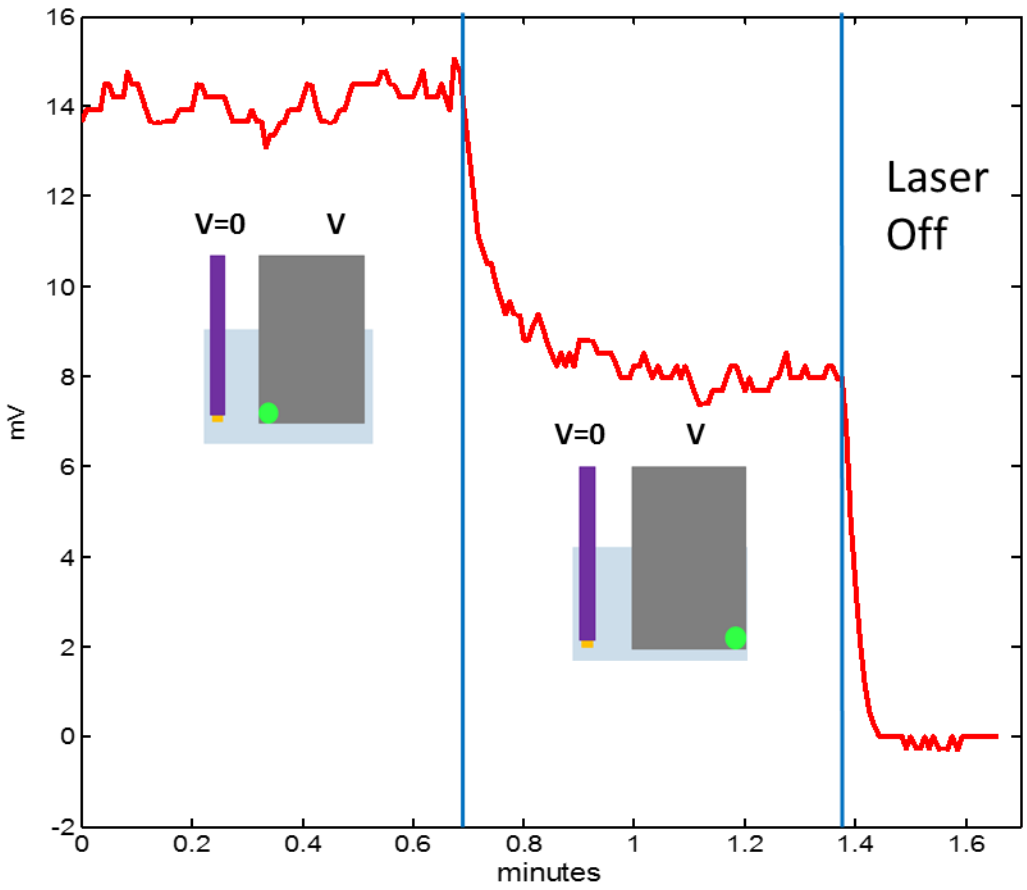

Figure 29: Voltage trace when using the green laser, deionized water, and the polarity of Au is (V=0) and the polarity of CuO is (V)

Experimental results with the 632 nm 1.2 mW red laser are shown in Figs. 30 and 31. In Figure 30, the voltage trace is acquired when the gold wire is positive (V) and the CuO is grounded (V=0). The polarities of the leads are reversed in Figure 30**.**

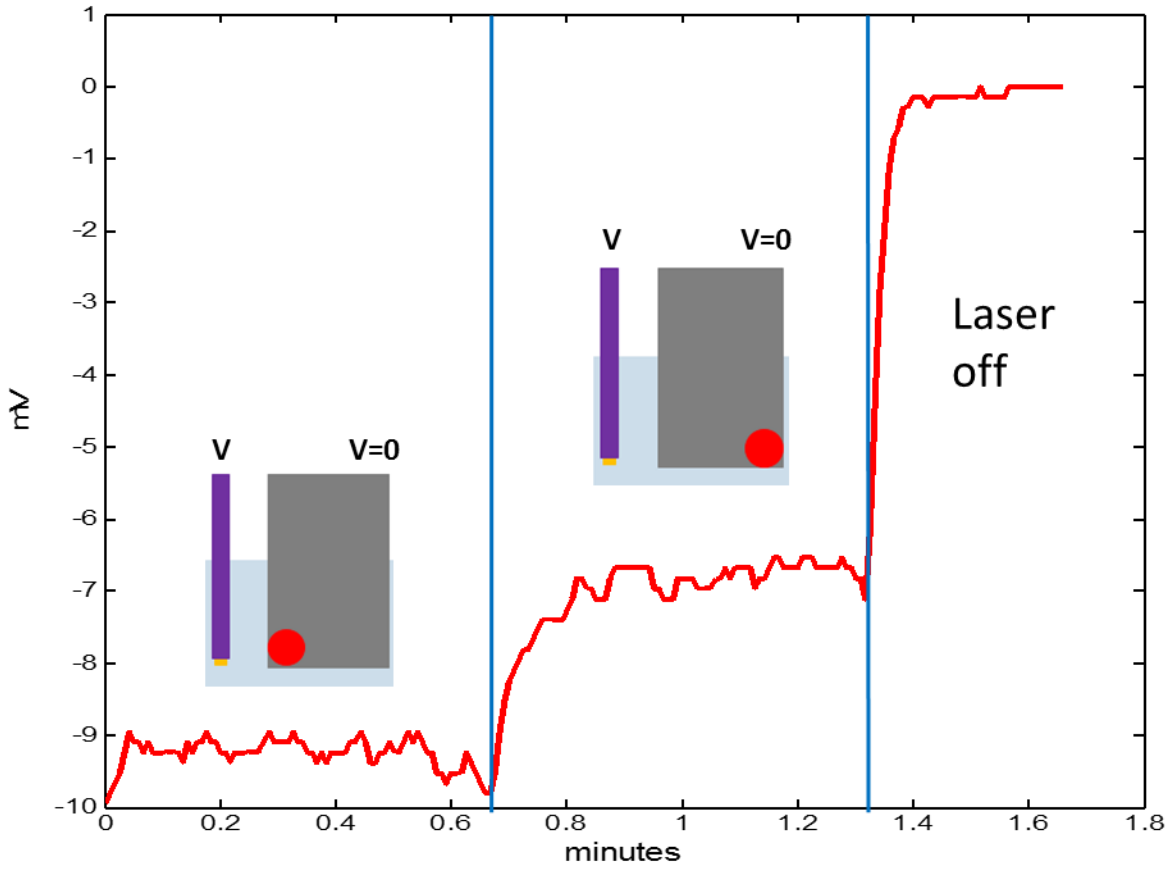

Figure 30: Voltage trace when using the red laser, deionized water, and the polarity of Au is (V) and the polarity of CuO is (V=0)

Notice the respective voltage outputs (-10mV and -7mV) are smaller for irradiation with the read laser compared to irradiation with the green laser (-14mV and -8mV) but it must be pointed out that this is not necessarily an effect of laser wavelength since the laser powers and spot sizes are different. It can also be seen that the distance from the laser spot to the gold wire as well as the polarity of the electrodes still have an effect on the output voltage.

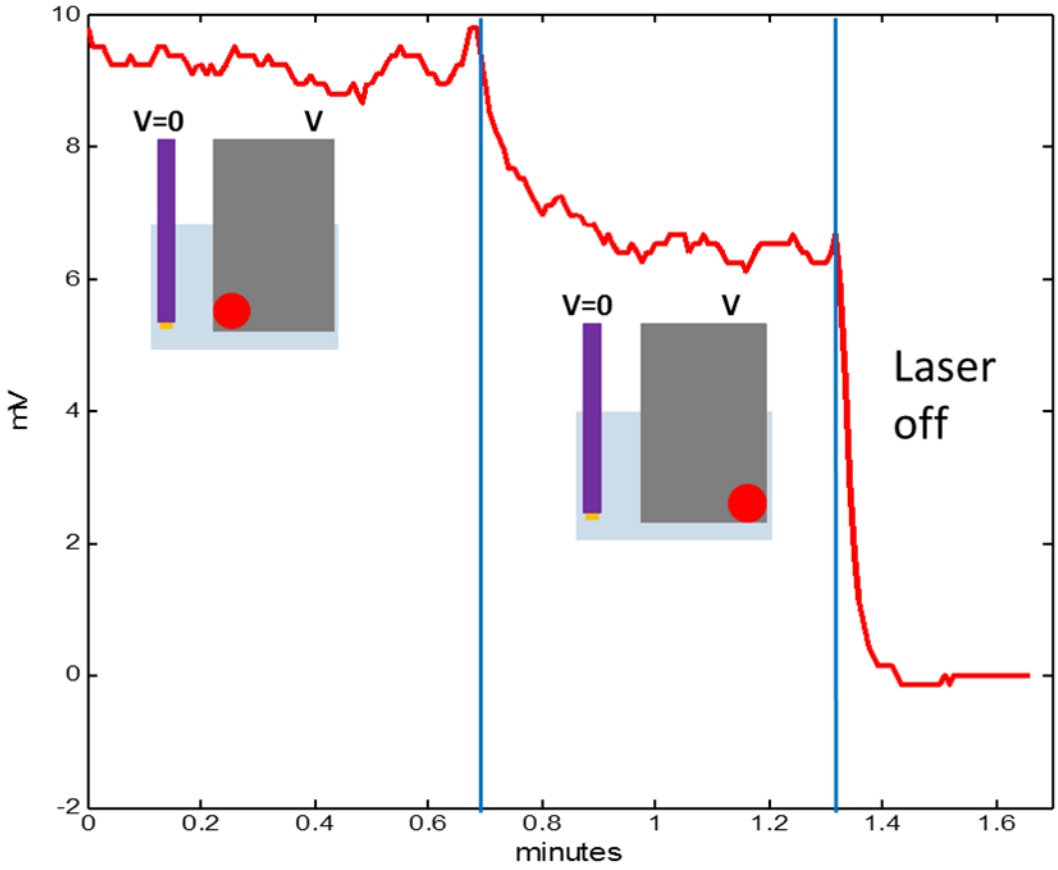

Figure 31: Voltage trace when using the red laser, deionized water, and the polarity of Au is (V=0) and the polarity of CuO is (V)

Direct measurements were also taken with a galvanometer in parallel with the voltage measurements in deionized water. There was no detectable current with the red laser, however, as can be seen in Fig. 32, the galvanometer shows a small current when the laser is turned off and then turned on to irradiate the lower left corner of the CuO sample. Each division on the scale is equal to 40nA.

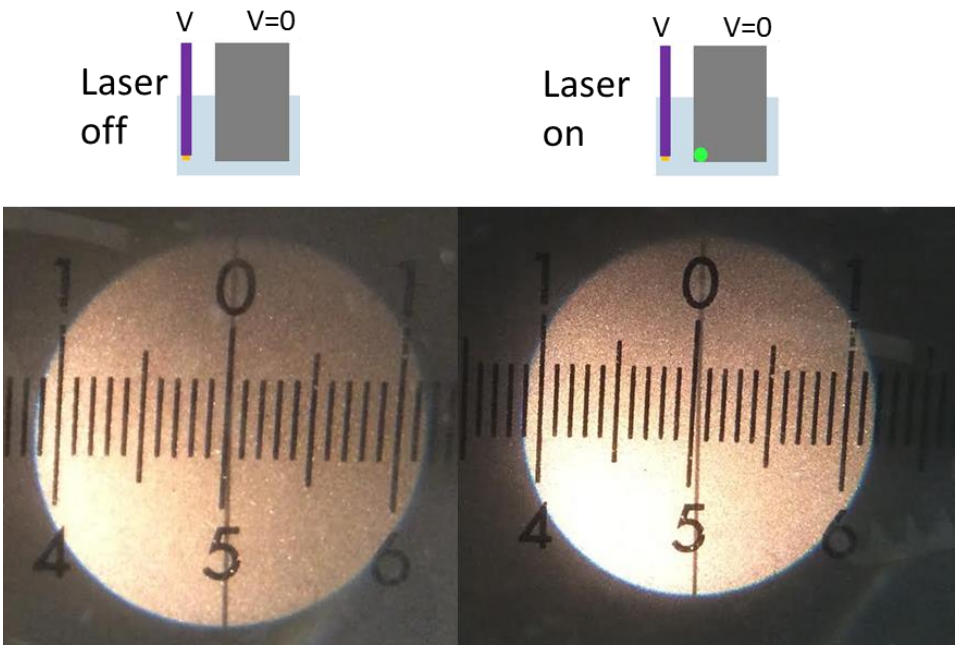

Figure 32: Measurement of current using a galvanometer. Experiment uses a green laser, deionized water, and the polarity of Au is (V) and the polarity of CuO is (V=0)

4.3.2) Buffer Solutions

In the buffer solution experiments the gold wire is grounded (V=0) and placed 5 mm from the positive (V) cupric oxide sample. First, an acidic solution monosodium phosphate (pH=4.32 @ 23.2C) is used as the solution and the steady state averages with range error bars can be seen in Figure 33. Figure 34 shows the steady state averages with range error bars for the alkaline solution, disodium phosphate (pH=9.13 @23.3C). Voltage was collected over a 45 second interval then averaged using MATLAB (Appendix C).

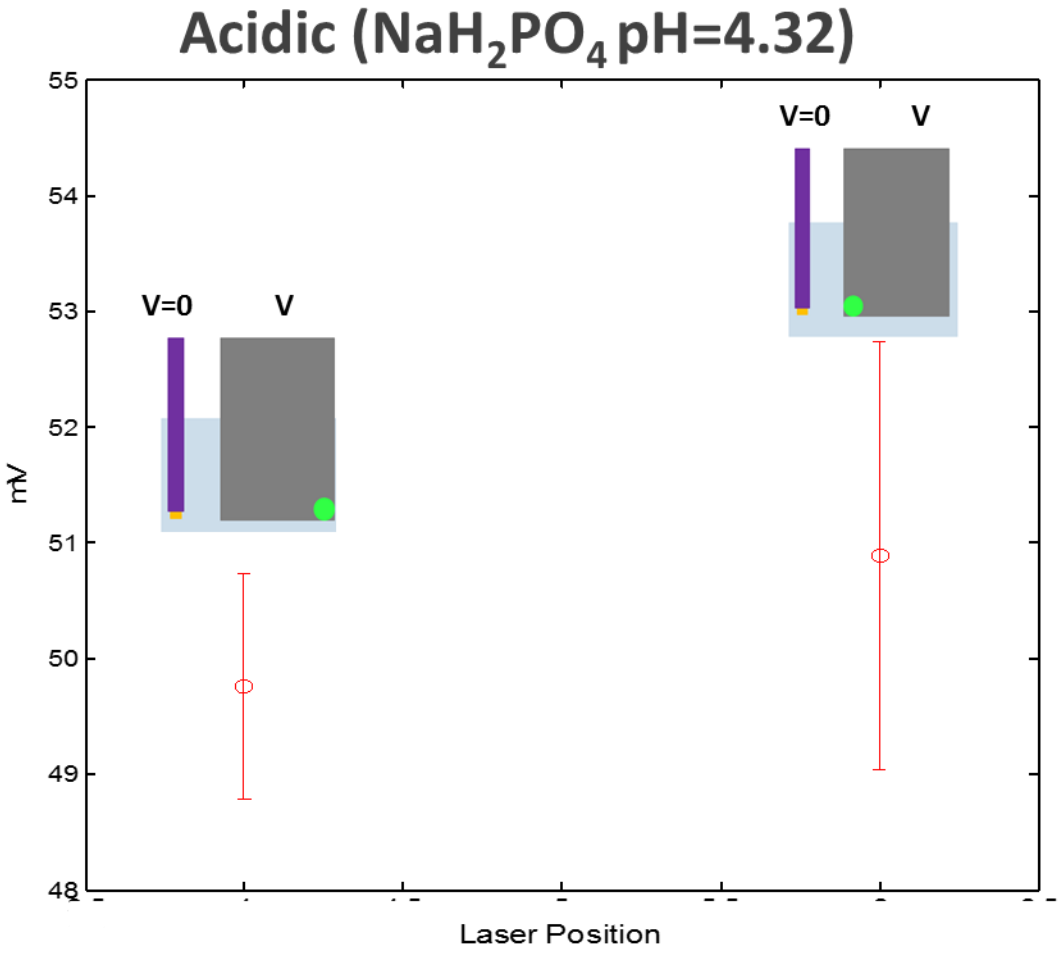

Figure 33: Voltage trace when using green laser, acidic solution (monosodium phosphate), and Au is (V=0) and CuO is (V)

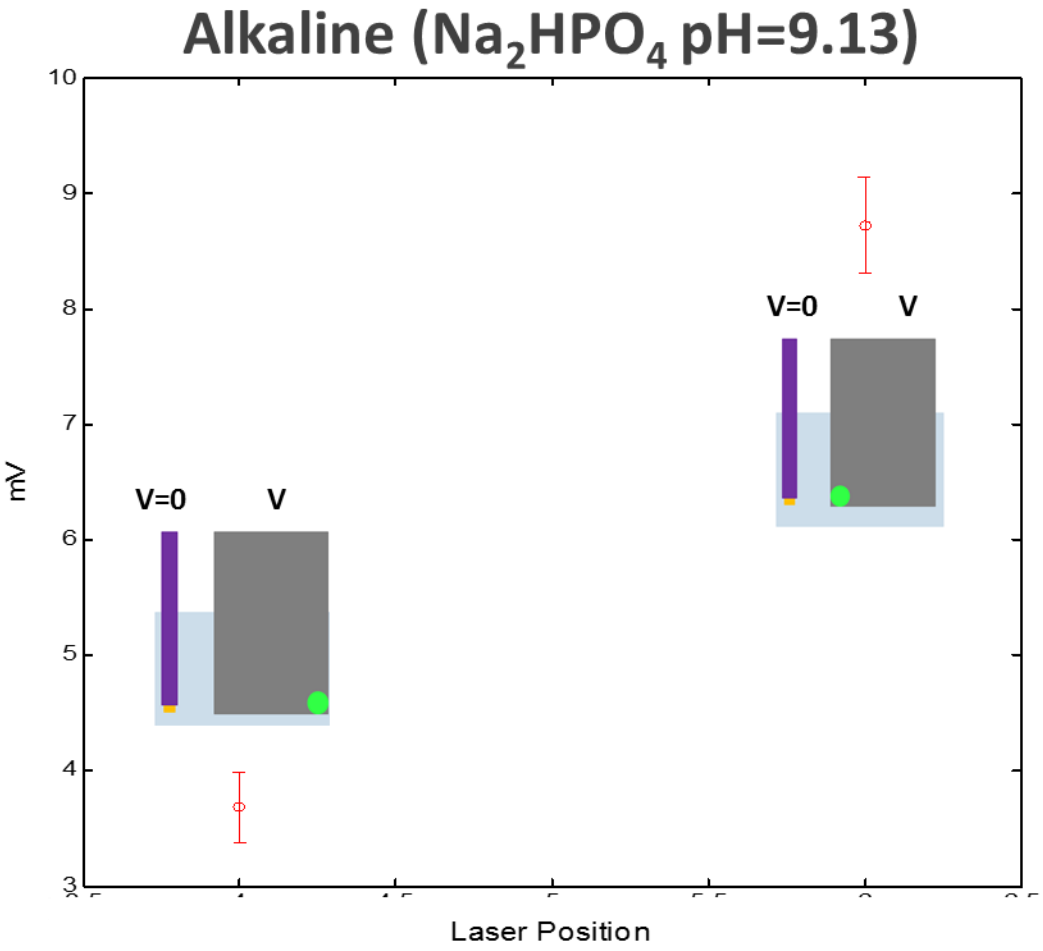

Figure 34: Voltage trace when using green laser, alkaline solution (disodium phosphate), and Au is (V=0) and CuO is (V)

Using a Keithley 2001 Picoammeter the current is measured for both buffer solutions. Table 3 shows the average of five trials where each individual trial was allowed to run for one minute.

Solution	Current (Amps)
NaH_2PO_4 (pH=4.32)	1.46 µA
Na_2HPO_4 (pH=9.13)	620 nA

Table 3: Current measured for the monosodium phosphate (pH=4.32) and the disodium phosphate (pH=9.13)

4.4) *Cupric Oxide Independent of Circuit*

In this set of experiments, the cupric oxide is placed between two equidistant gold wires shown in Figure 35 and is **not** part of the circuit. Green and red laser irradiation is used and only deionized water serves as the solution in these experiments.

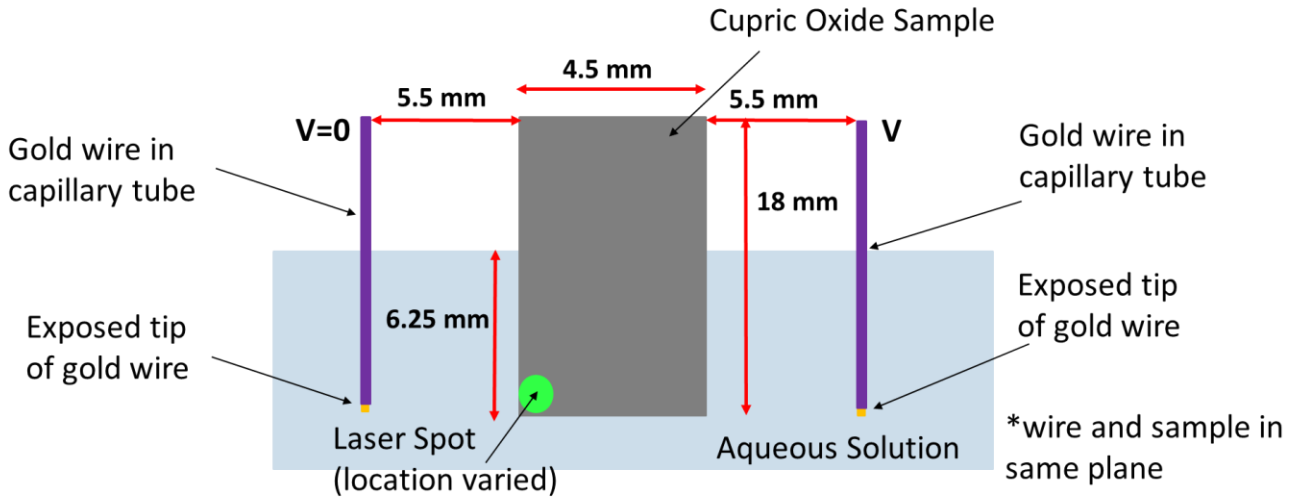

Figure 35: Diagram of gold wire leads and CuO sample independent of circuit

Figure 36 shows the continuous voltage trace when the green laser illuminates the CuO sample. The laser spot is initially above the water line and no voltage is detected. The laser spot is then directed below the water line equidistant between the two gold wires and still no voltage is detected. Once the laser spot moves closer to the positive (V) gold lead the signal becomes negative. As the laser spot is moved closer to the positive exposed gold wire tip, the voltage output becomes more negative. When the laser spot is equidistant from both gold wires and the signal goes back to zero as in the case of the experiments with the green laser. Then the signal rises to its maximum positive voltage when it is closest to the grounded (V=0) gold lead and decreases to a smaller positive voltage when moved up the sample. The voltage trace in Figure 37 utilizes the red laser and shows the same effects but with smaller voltage outputs.

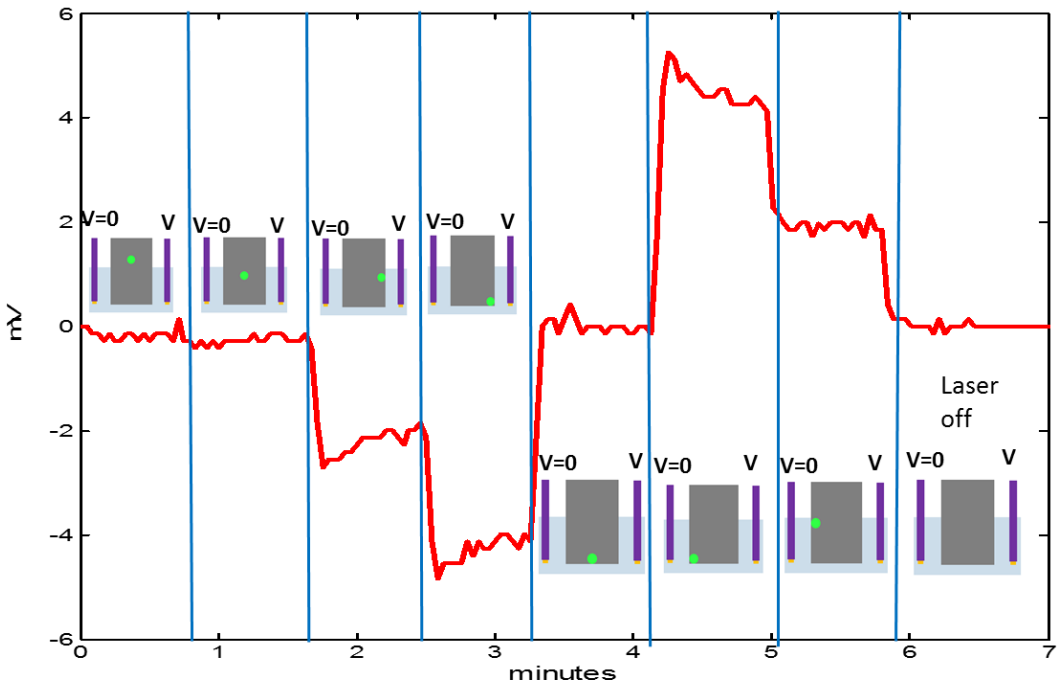

Figure 36: Voltage trace using green laser, deionized water, and CuO is independent of circuit

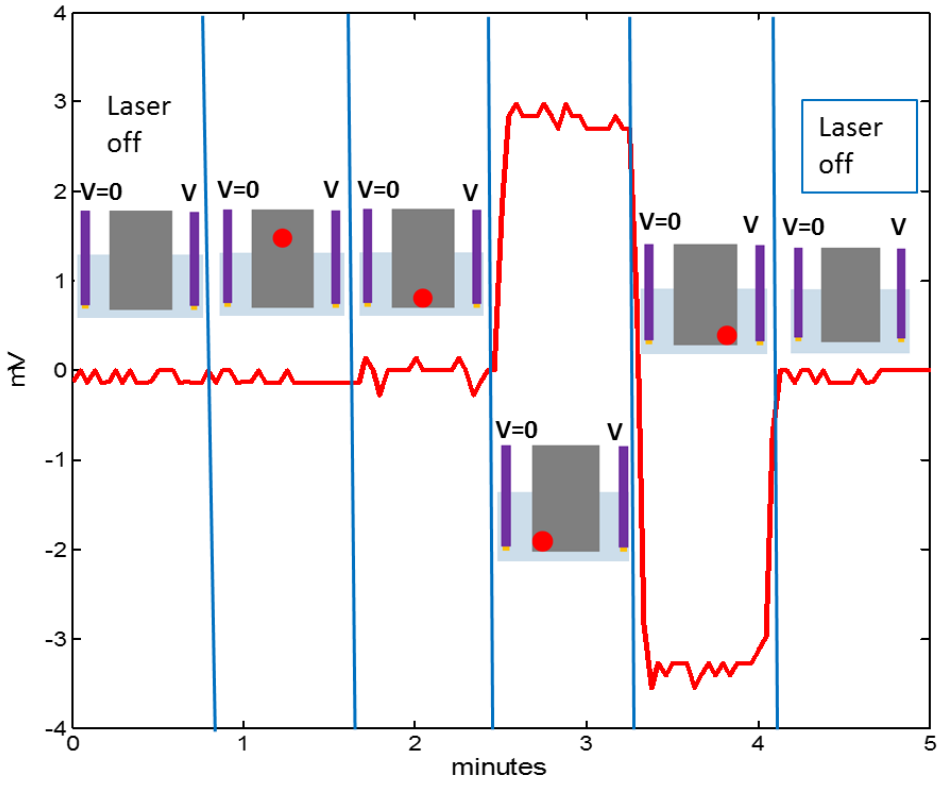

Figure 37: Voltage trace using red laser, deionized water, and CuO is independent of circuit

4.4.1) *Effect of Varying Distance between Gold Wire Lead and Laser-irradiated Spot on CuO Electrode on Photoelectrochemical voltage*

In the previous experiments, it was shown that the farther away the laser spot is from the exposed tip of the gold wire lead, the smaller the photoelectrochemical voltage. The voltage dependence on distance is investigated further in additional experiments.

The (7mm x 18mm) laser-irradiated cupric oxide foil is **not** part of the circuit, deionized water is used, and the green laser irradiates the lower left corner of the sample. The negative gold

lead (V=0) is initially located 1mm away from the sample edge and then incrementally positioned farther away from the sample. The five distances used are 1mm, 2mm, 5mm, 10mm and 15mm.

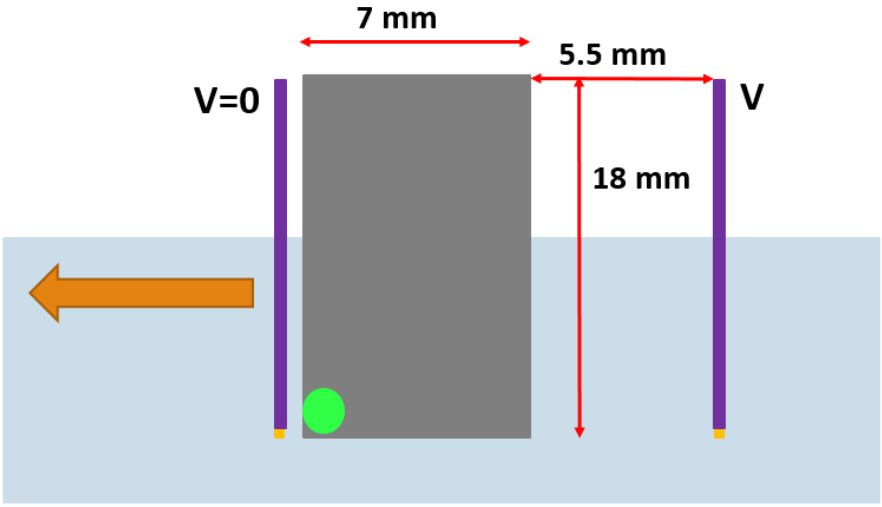

Figure 38: Diagram of experimental setup for distance experiments

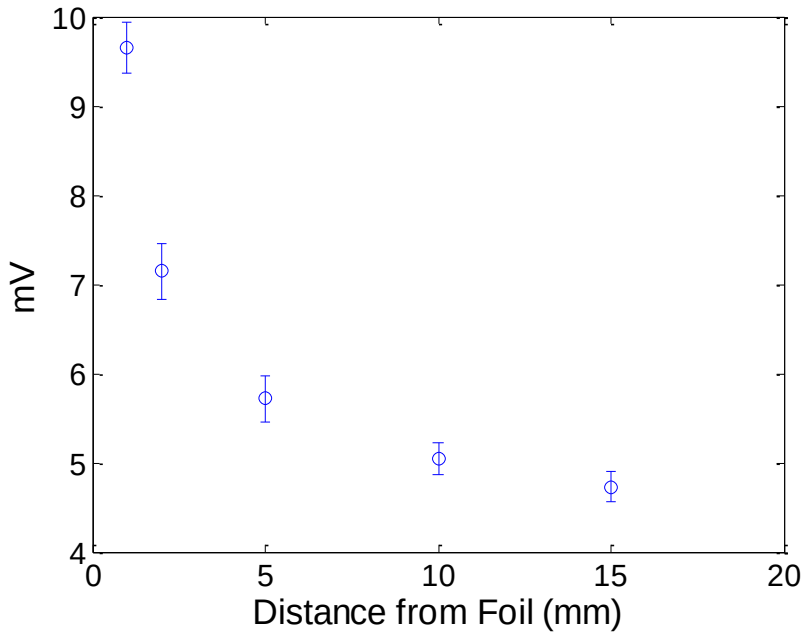

Figure 39: Distance from foil vs Voltage output

Figure 39 shows the steady state voltage averages with error bars (based on range of values) as a function of distance. Figure 40 shows the two term exponential used to curve fit the data. Curve fitting was performed using MATLAB's built in curve fitting tool (cftool). The physical implications of the two terms are discussed at the end of this section.

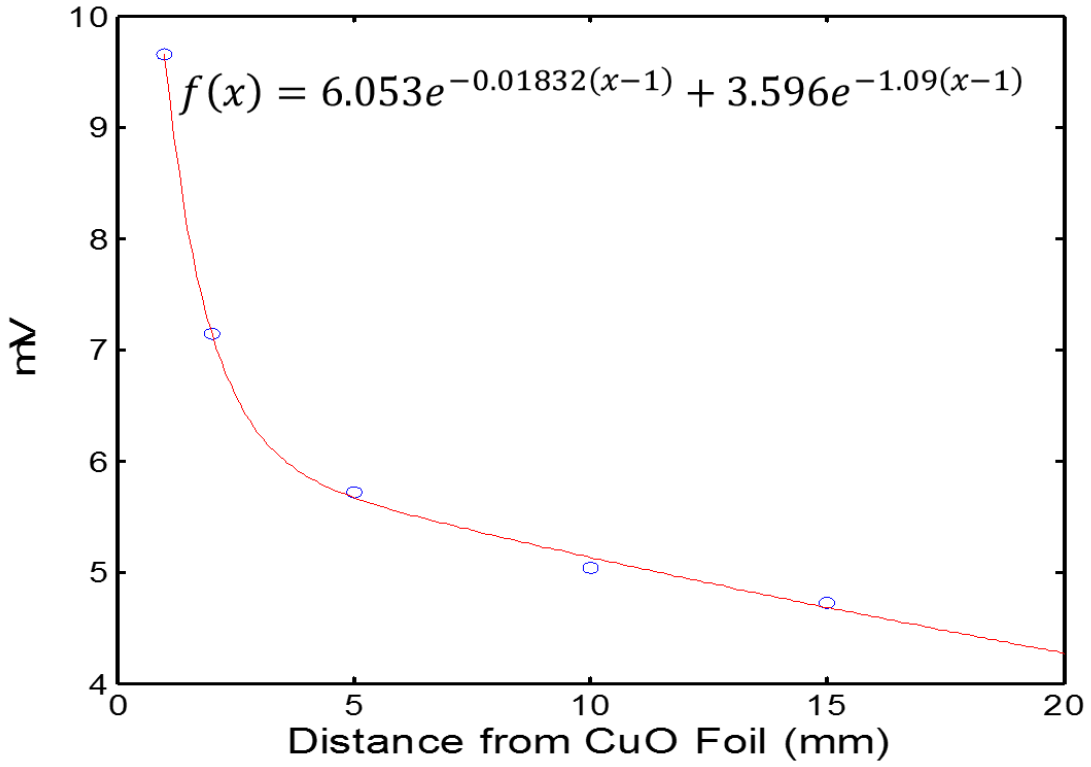

Figure 40: Curve fit for distance from foil vs voltage output

4.4.2) *Ranging pH Experiments*

To determine the pH at which the voltage output is largest when the cupric oxide is not part of the circuit, five solutions on both sides of pH=7 are prepared. Table 4 shows the amounts of monosodium phosphate, disodium phosphate, and deionized water mixed together to create each pH.

pH	NaH_2PO_4 (pH=4.32)	Na_2HPO_4(pH=9.13)	Deionized Water (pH=7.4)
4.32	20 mL	0	0
6.5	7.35 mL	2.65 mL	10 mL
7	5.1 mL	4.9 mL	10 mL
7.5	2.8 mL	7.2 mL	10 mL
9.13	0	20 mL	0

Table 4: Amounts of monosodium phosphate, disodium phosphate, and deionized water to prepare each solution

Three (4.5mm x 18mm) cupric oxide samples are used for the experiments. The first cupric oxide sample is used for pH < 7, the second is used for pH=7, and the third is used for pH > 7. Only deionized water is used and the green laser irradiates the lower left corner of the sample closest to the grounded gold wire.

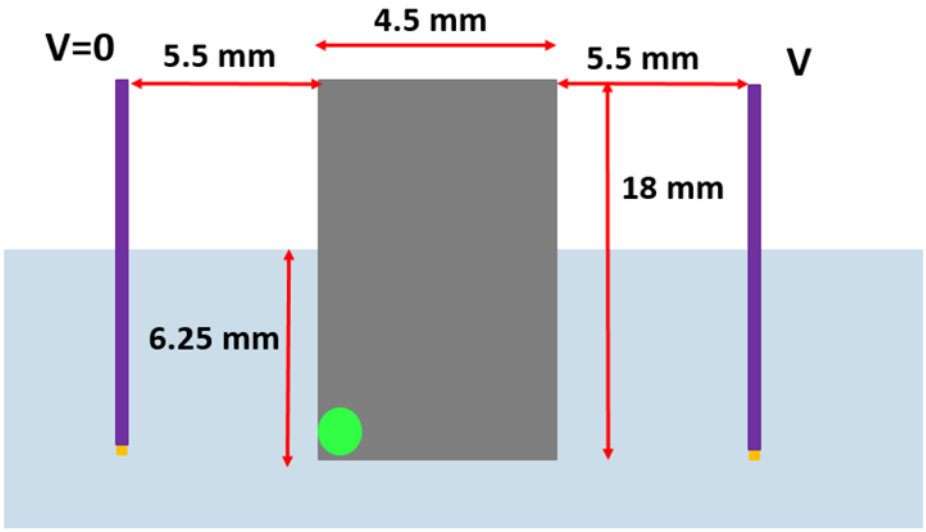

Figure 41: Diagram for ranging pH experiments

Figure 42 shows the steady state voltage averages with error bars for each pH. The maximum voltage occurs at a pH of 7.5 but it is important to note that the voltage output is greater in acidic solutions than alkaline solutions, consistent with what Becquerel reported in 1839 with the irradiated electrode being part of the circuit.

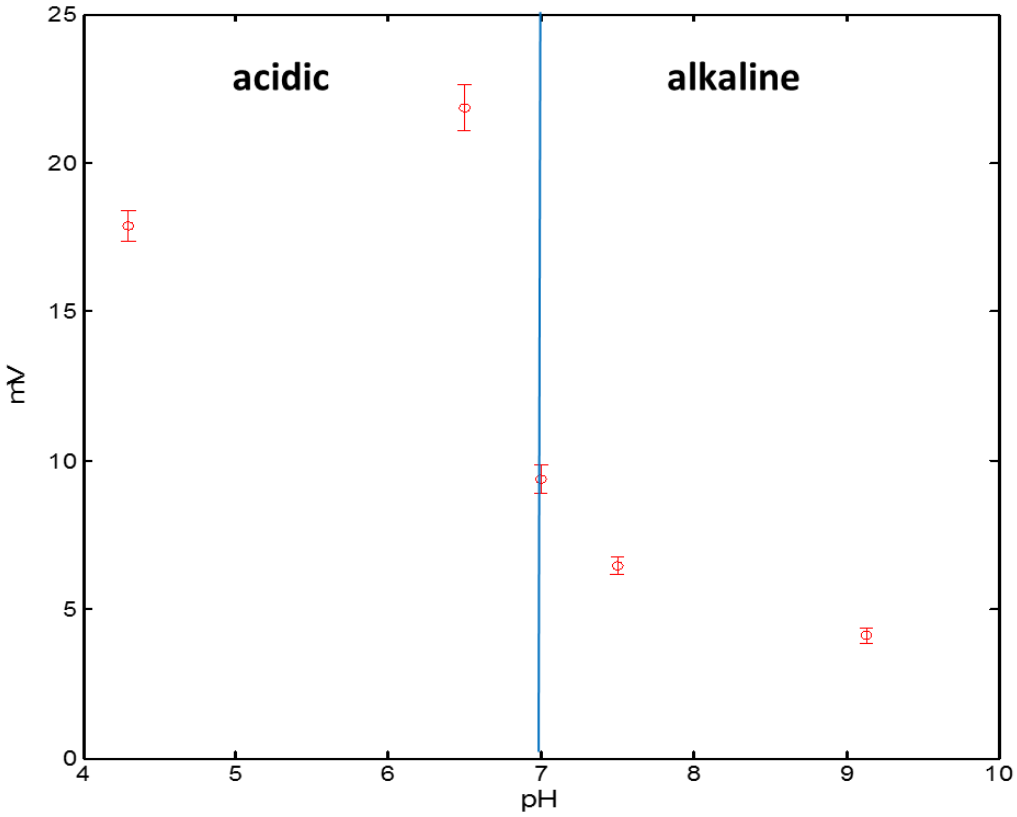

Figure 42: pH of solution vs voltage output

4.5) *Summary of Photoelectrochemical Experimental Results*

There are five consistent effects seen throughout all of the photoelectrochemical experiments.

Result 1: The sign of the voltage output depends on whether the laser position is closer to the grounded gold wire (V=0) or the positive gold wire (V). In the first case the output voltage is positive and in the ladder case the output voltage is negative.

Result 2: The magnitude of the voltage output depends on the distance between the laser position and the adjacent gold wire.

Result 3: Acidic solutions produce higher voltage and current outputs than alkaline solutions.

Result 4: The 532nm 14.3mW green laser produces larger voltage and current outputs then the 632nm 1.2mW red laser.

Result 5: Current is measured when the sample is part of the circuit and is not detected or is negligible when the sample is not part of the circuit. Voltage is measured in both scenarios but larger voltages are seen when the sample is part of the circuit.

4.6) *Possible Explanation for Photoelectrochemical Effect*

Before formulating a plausible theory as to what may occurring in the experiments reported here, it is important to review the physics and chemistry of the process before the laser irradiates the surface. First, by burning the pure copper foil in air, a layer of cupric oxide (CuO) is formed that likely contains crystal imperfections. It is well-known that cupric oxide is a p-type semiconductor. In a p-type semiconductor acceptor energy levels are present just above the

valance band. As a result valence electrons with enough energy can occupy these acceptor energy levels. Before any additional energy is added to the sample by laser light, there are already electrons that have sufficient enough thermal energy to occupy acceptor levels. In turn, these electrons leave a hole in the valence band.

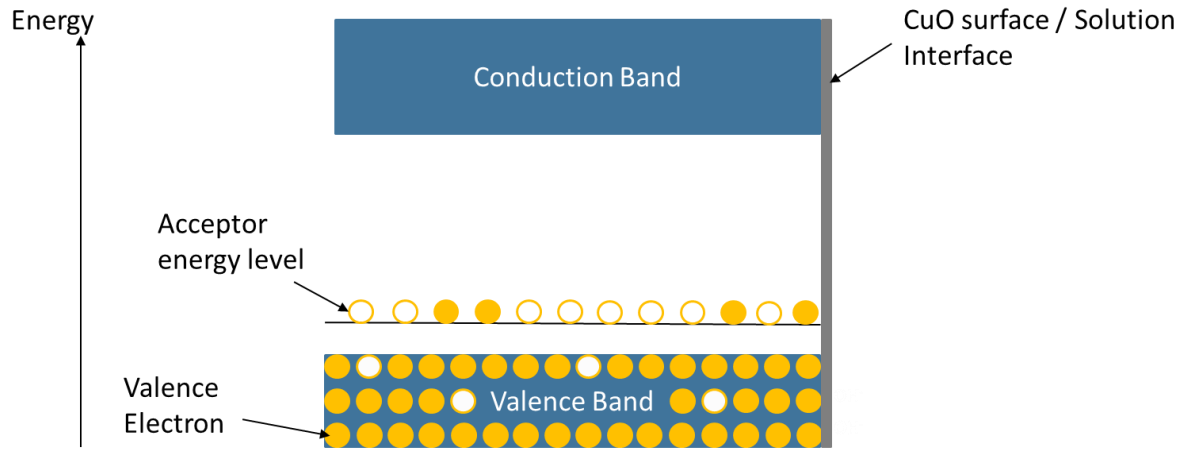

Figure 43: Energy levels of CuO (p-type semiconductor)

There are many different ways in which the electron can be supplied with enough energy to move out of the valence band but in the present case we are primarily concerned with laser light. Both the green 532 nm and red 632 nm lasers used in these experiments have photon energies of 2.33 eV and 1.96 eV, respectively, which is sufficient energy to allow the electrons to occupy the acceptor energy levels.

$$E = h(\frac{v}{\lambda}) \quad \textbf{(18)}$$

where, E= quantum energy of photon (eV), h =Planck's constant = 4.136 x 10^{-15} (eVs), v = speed of light = 3x10^{8} m/s, and λ = wavelength of light (m).

The other integral aspect of the system is the fact that the sample and wires are immersed in an electrolyte solution. The main ion of interest is the hydroxide (OH-) ion because it is present in both the deionized water and the buffer solutions. In deionized water, there are a hydronium (H_3O^+) and hydroxide (OH-) ions present. These hydroxide and hydronium (H_3O^+) ions are constantly recombining to form water. Conversely, to keep the system at equilibrium, water molecules can donate or accept hydrogen ions (H+) which produces hydronium and hydroxide ions:

$$H_3O^+ + OH^- + M \rightarrow H_2O + H_2O + M \quad \textbf{(19)}$$

For the acidic and basic solutions, monosodium phosphate (NaH_2PO_4) and disodium phosphate (Na_2HPO_4), it is true that Na^+ and PO_4^{-3} ions are also present but the amount of hydronium ions dictates the pH of the solution (Equation 20). Equations 21 and 22 dictate the concentration of ions in each buffer solution and ensure overall charge neutrality in the solution.

$$[H_3O^+] = 10^{-pH} \quad \textbf{(20)}$$

Acidic NaH_2PO_4:

$$n_{H_3O^+} = n_{PO_4^{-3}} + n_{OH^-} \quad \textbf{(21)}$$

Alkaline Na_2HPO_4:

$$n_{OH^-} = n_{H_3O^+} + n_{Na^+} \quad (22)$$

All possibilities necessary to explain all five results observed in the photoelectrochemical experiments are now considered. As the copper oxide is placed in the solution, hydroxide ions begin to adsorb on to the surface because of the presence of holes in the valence band.

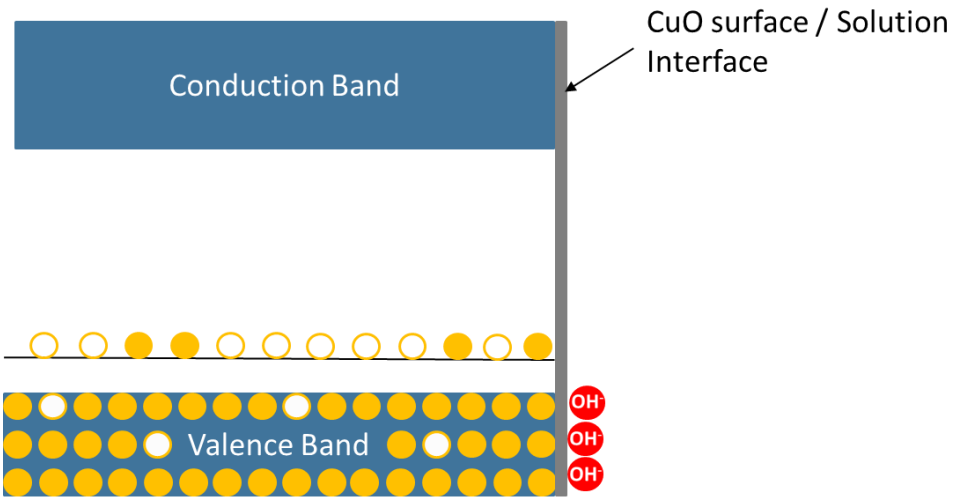

Figure 44: Hydroxide ions adsorbing to the surface of the CuO sample

Once the laser irradiates the surface of the cupric oxide there are two possible scenarios that could occur:

1) Additional electrons could move out of the valence band and into the acceptor energy levels causing more hydroxide ions to adsorb to the surface.
2) Hydroxide ions could desorb from the surface of the cupric oxide and transfer their charge through the solution.

If the first scenario is the dominant mechanism, then the adsorption of more hydroxide ions onto the cupric oxide surface would result in residual positive charge in the adjacent gold wire. If the second scenario is the dominant mechanism, then desorbed hydroxide ions near the adjacent gold would result in an overall negative potential around gold wire. The second scenario complies with the first experimental result in chapter 4.5 while the first scenario does not. Figure 45 shows that when hydroxide ions are in the vicinity of the Au (V=0) lead, the voltage is locally negative with respect to the Au (V) wire. This results in the grounded lead, Au (V=0), becoming more negative with respect to the positive lead, Au (V), thus creating a positive output voltage. In the case shown in Figure 46, when hydroxide ions are near the Au (V) lead, the Au (V) lead becomes negative with respect to the Au (V=0) lead, which results in a negative output voltage.

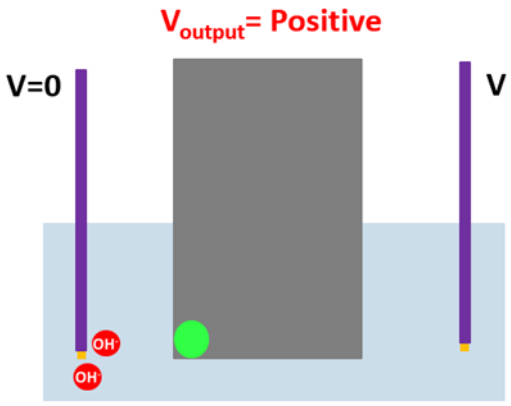

Figure 45: Hydroxide ions near grounded (V=0) gold lead which results in a positive output voltage

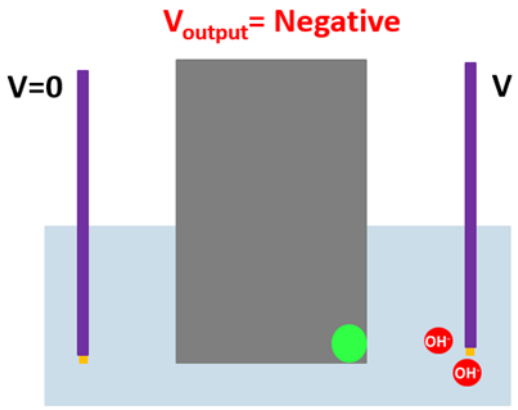

Figure 46: Hydroxide ions near positive (V) gold lead which results in a negative output voltage

The experiments also show that when the laser is directly in the middle of the sample, there is little voltage to be seen. In this case, the hydroxide ions are equally distributed to each lead resulting in a net zero voltage.

As the laser continuously irradiates the surface of the sample, hydroxide ions continually are desorbed from the surface and transfer their charge outward until they recombine with a hydronium ion or reach an electrode. The Grotthuss mechanism describes the mechanism by which the hydroxide ion transfer their charge through water. The Grotthuss mechanism describes water molecules rotating their orientation to accommodate and propagate the hydroxide ion and in a sense act like a daisy chain [12].

Figure 47 shows the propagation of the hydroxide ion through water. The oxygen atom of the hydroxide atom (initially coupled to the water molecule through hydrogen bonds) detaches one of the hydrogen atoms on the water molecule which turns the water molecule into a hydroxide ion.

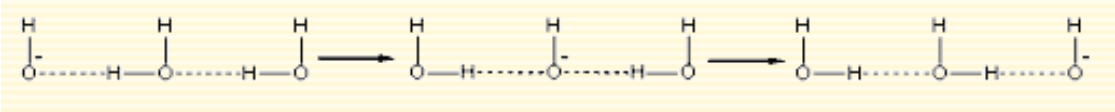

Figure 47: Shows how hydroxide transfers charge through water using Grotthus mechanism

The second experimental result stated in chapter 4.5 shows that as you move the gold wire farther away from the cupric oxide sample, the voltage output decreases. This is probably due to the fact the some hydroxide ions collide with hydronium ions and form water and only some hydroxide ions make it to the gold wires.

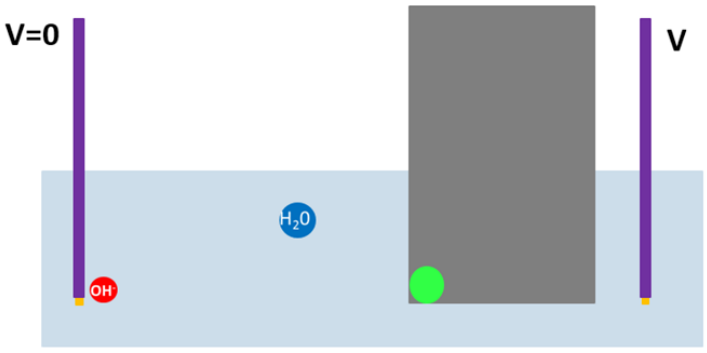

Figure 48: Some hydroxides collide with hydronium ions to form water

In the experiments where the gold wire is incrementally moved farther from the sample a two term exponential is best suited to curve fit the data and can provide some insight to exactly what is occurring on a microscopic level. This two term exponential, shown in Equation 23, hints at the idea that the effect as a whole is governed by two submechanisms operating together. Figure 49 shows how each of the exponentials dominates a certain distance range.

$$\boldsymbol{Voltage(x) = f(x) = 6.053e^{-.01832(x-1)} + 3.596e^{-1.09(x-1)}} \qquad \textbf{(23)}$$

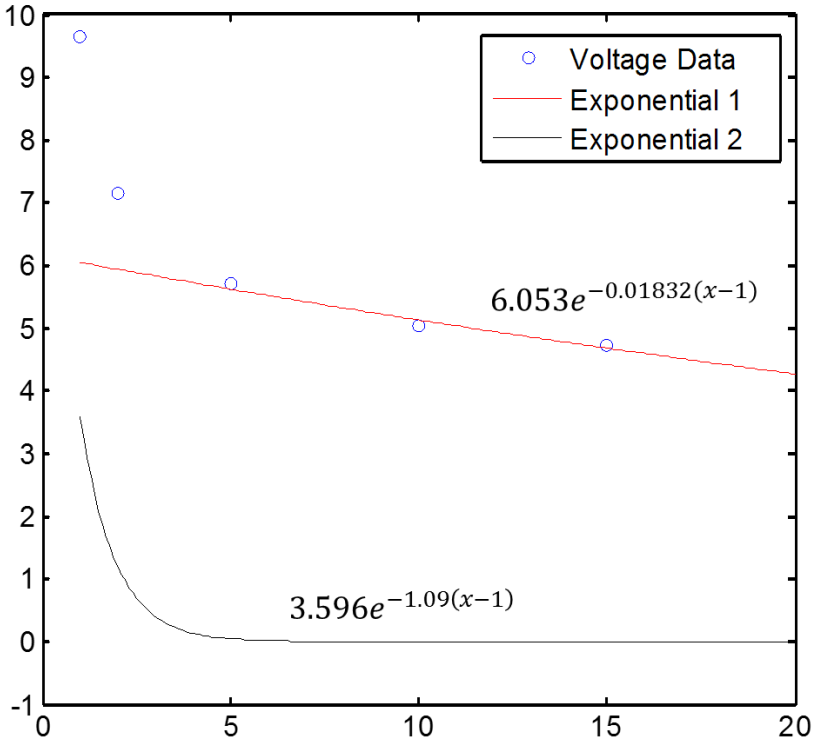

Figure 49: Curve fit split into two exponentials each displaying a different physical mechanism

It is possible that the first mechanism (indicated by Exponential 2 in Fig. 49) occurs within the very close ranges from the cupric oxide and the second (Exponential 1 in Fig. 49) operates within a larger centimeter scale from the surface. This could be indicative of the existence of a space charge layer or sheath in the vicinity of the irradiated sample. As hydroxide ions are desorbed from the surface, a negative space charge must develop in order to keep the entire solution quasi-neutral. The two exponentials are likely indicative of the sample-adjacent sheath and the longer transfer of charge from the irradiated sample to the collection electrode.

This hydroxide sheath also assists in developing a plausible theory for why acidic solutions produce higher voltage and currents then alkaline solutions as stated in the third result of chapter 4.5. In acidic solutions there is are more positively charged hydronium ions that negatively charged hydroxide ions. This abundance of positive ions could be attracting hydroxide ions from within sheath and therefor make it easier for them to tranfer their charge outwards. In alkaline solutions the opposite is true. There is an abundance of hyrdoxide ions that are repelling hydrioxide ions thus making it harder for them to transfer their charge outwards.

Result 4 in chapter 4.5 states that in every experiment the green laser produced a higher voltage output then the red laser. The fact that this is occurring could be a consequence of the intensity of each laser. Intensity is defined as power divided by surface area the laser irradiates. The green laser spot diameter is approximately half the size as the red laser (1.5 mm: 3.25mm) and the power of the green laser is far greater than the red (14.3 mW: 1.2 mW). This results in an intensity of 8.09 mW/mm^2 for the green laser and a 0.145 mW/ mm^2 for the red laser. The larger intensity of the green laser could mean that it is desorbing a larger amount of hydroxide ions.

Result 5 states that current is not detected when the cupric oxide is not part of the circuit which could be because there is no mechanism in which the hydroxide ion can donate an electron to the gold wire. When the cupric oxide sample is part of the circuit electrons-hole pairs are free to move throughout the circuit.

Chapter 5

Conclusions and Recommendations for Future Work

5.1) *Interpretation of Electrical Signals from Organoid Experiments*

The electrical activity seen in the organoid experiment is promising and strongly suggests that there is intrinsic electrical activity in these organoids. Still, after conducting experiments on the cupric oxide and gold electrodes it would be incorrect to assume the organoid is solely responsible for the electrical activity without first analyzing the experiment and considering the photoelectrochemical phenomenon. First and foremost, the organoid was illuminated with the green 532nm 14.3 mW laser and a burnt copper wire was puncturing the organoid, there is a possibility that the wire had been illuminated by the laser. In addition, the HBSS solution that the organoid sat in had a pH of 7.4 and the burnt copper electrode and gold wire were in close proximity of each other (<5mm). Considering that the control experiments showed a significant voltage output in these conditions the photoelectrochemical phenomenon could have had an impact on the voltage output that was measured.

Despite the possibility of the photoelectrochemical effect having a significant impact on the voltage trace, there are still some peculiar characteristics of the voltage trace that should be considered. First, the transient response is approximately a minute long which is longer than any response seen the photoelectrochemical phenomenon experiments. Second, after the glutamate blockers are added and the laser is still on at position “5” indicated in Figure 50, the signal drops to 4 mV instead of the original 2mV. This additional 2 mV could be due to the photoelectrochemical effect. Furthermore, the voltage rise seen when the laser is illuminating the

organoid and glutamate blockers have not been added yet, from position “2” to “3”, could be the result of an additive effect between the photoelectrochemical effect and the organoid exhibiting electrical activity.

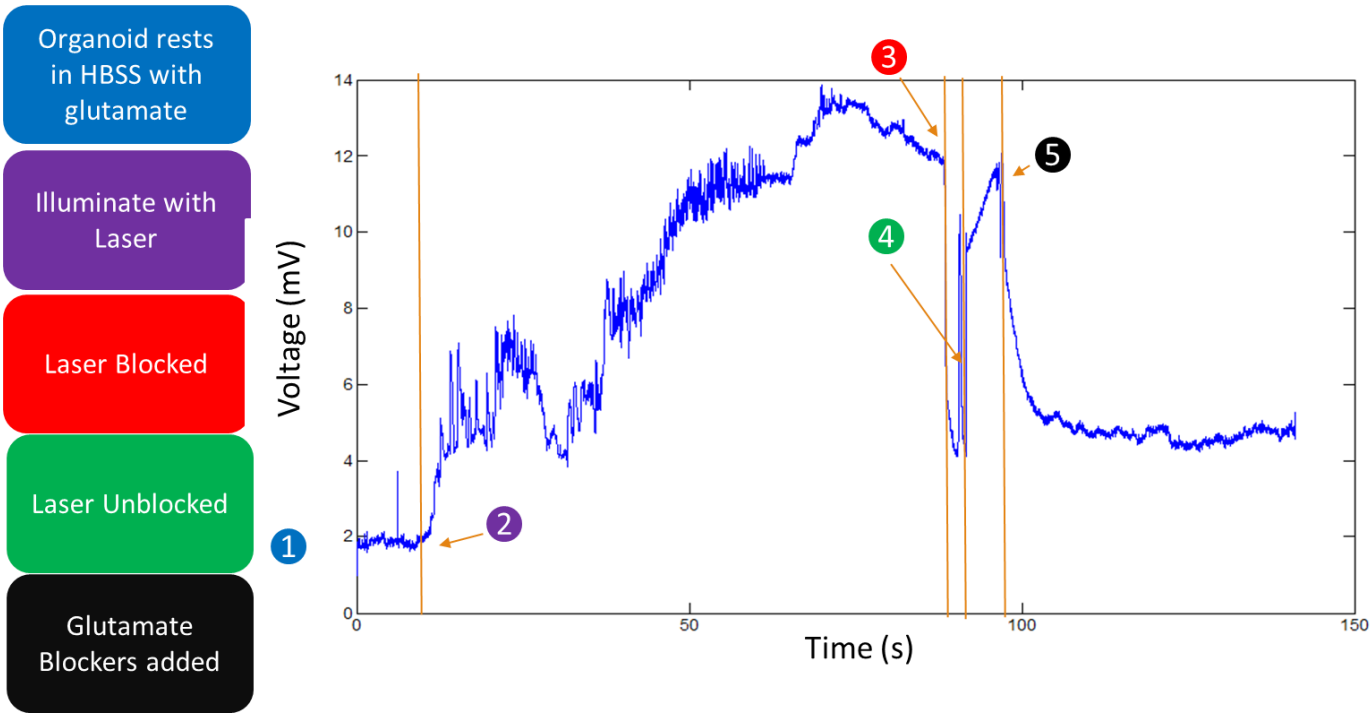

Figure 50: Organoid Voltage trace with indicators

5.2) *Recommendation for Future Work - Electromagnetic Detection*

Cerebral organoids are still a very new technology and there is a plethora of research that could be conducted pertaining to electrical brain activity detection. It is necessary to conduct more experiments on these organoids to attempt to replicate the electrical response and gain a better insight to whether or not the organoid has the ability to emit collective oscillations akin to the alpha, beta, delta, and theta waves typically observed in human brains

The electromagnetic probe will continue to be optimized for the detection of electrical activity from cerebral organoids. In addition, it is possible that an array of these coils could be used further to study neural network connectivity in the organoids and provide further insights to the maturity of these cerebral organoids as they develop. An "electrical map" demonstrating the neural connectivity within the organoid could help identify if there are regions within the organoid that possess EM activity much like the different regions in an actual human brain.

5.3) *Photoelectrochemical Effect – Further Applications*

The photoelectrochemical phenomenon has strong implications for the development of a photogalvanic solar cell. The need for renewable energy sources such as solar power is apparent when one considers the overwhelming use of coal and oil and the impacts that they have on the environment. The use of solid state photovoltaic (PV) solar cells for solar energy has dominated the latter of the 20^{th} century but with the over 70 percent of the globe covered in oceans it would be beneficial to develop a solar cell that utilizes an aqueous solution. Currently the main obstacle facing the development of this type of photogalvanic cell is corrosion due to oxidation – reduction reactions [13]. Although only an extremely small current was produced in deionized water when the sample was part of the circuit, no corrosion will occur because only water is present. Furthermore, cupric oxide is relatively inexpensive at 2-12$ per kilogram while the price of regular grade silicon (the main semiconductor in PV solar cells) is around 500$ per kilogram. With the price of silicon being considerably higher than cupric oxide, there is a clear incentive to continue researching this photoelectrochemical phenomenon.

References

[1] Lancaster, M.A. et al.(2013) Cerebral organoids model human brain development and microcephaly. *Nature* 501, 373-379.

[2] D. K. Ahirwar, M. W. Nasser, T. H. Jones, E. K. Sequin, J. D. West, T. L. Henthorne, J. Javor, A. M. Kaushik, R. K. Ganju, and V. V. Subramaniam, "Non-contact method for inducing electrotaxis," accepted for publication in Scientific Reports, 2015.

[3] J. Banerjee, P. D. Ghatak, S. Roy, S. Khanna, E. K. Sequin, K. Bellman, B. C. Dickinson, P. Suri, V. V. Subramaniam, C. J. Chang, and C. K. Sen, "Improvement of Human Keratinocyte Migration by a Redox Active Bioelectric Dressing", PLoS One, Vol. 9, No. 3, p. e89239, March 2014.

[4] A. Samin, and V. V. Subramaniam, "Analytical Solutions to the Steady State Poisson-Nernst-Planck Equations in Electrobiochemical Systems", Applied Physics Research, Vol. 7, No. 2, pp. 40-48, 2015.

[5] "What Is Magnetoencephalography?" *Institute for Learning & Brain Science*. University of Washington, n.d. Web

[6] R. M. W. Collins, "Physics of Potassium Ion Channel Inactivation in Neurons", American Journal of Undergraduate Research, Vol 3. No. 1, pp 27-36, 2004

[7] B. J. Roth, and J. P. Wikswo, "The magnetic field of a single axon: A comparison of theory and experiment", Biophysics Journal, Vol. 48, pp.93-109, 1985.

[8] E. K. Sequin, "Effects of Induced Electric Fields on Tissues and Cells", Ph.D. Dissertation, The Ohio State University, Summer 2014.

[9] "What Are Brain Waves?" *Transparent Corporation - Brainwaves Overview*. N.p., n.d. Web. 27 Nov. 2015.

[10] W. J. D. Van Dijck, “The Becquerel-effect on copper oxide electrodes”, Transactions of the Faraday Society, Vol. 21, pp. 630-636, 1925.

[11] A. Wallace Copeland, Otis D. Black, A. B. Garrett, “The Voltaic Effect”, Department of Chemistry, The Ohio State University, Summer 1941.

[12] Chaplin, Martin. "Grotthus Mechanism." *Water Structure and Science*. N.p., n.d. Web. 20 Nov. 2015.

[13] W.W. Anderson, and Y.G. Chai, “Becquerel Effect Solor Cell”, Energy Conversion, Vol. 15, pp. 85-94, 1976.

[14] McFerran, J. L., *An Electromagnetic Method of Cancer Detection*, Ph.D. dissertation, The Ohio State University, 2009.

[15] Travis H. Jones, Ph.D. Candidate, Applied Physics Laboratory, Department of Mechanical & Aerospace Engineering, The Ohio State University, personal communication, November 2015.

Appendix A

MATLAB Circuit Element Calculation

```
%This program calculates mutual inductances between coils,
%self-inductances of the coils, and resistances the coils

% Inputs:
%         [L] Length of probe, m
%         [dw] diameter of wire used to construct probe,
%         [d1d] inner diameter driver coil, m
%         [d2d] outer diameter driver coil, m
%         [D2r] inner diameter reciever coil, m
%         [D3r] outer diameter reciever coil, m
%         [D] number of turns in r-direction (layers), driver coil
%         [M] number of turns in r-direction (layers), reciever coil
%         [Nd] number of turns/layer, driver coil
%         [Nr] number of turns/layer, reciever coil
%         [freq] driving frequency, hertz (used to calc loop resistance)

% Outputs:
%         [Ld] Self inductance Primary coil, H
%         [Lr] Self inductance Detector coil, H
%         [M_dr] Mutual inductance from driver(primary) to receiver
%              (detector), H
%         [M_rd] Mutual inductance from the receiver to driver, H


%ADDED INPUTS
%         [ro] Resistivity of Copper


function [Ld, Lr, M_dr, M_rd, Rd, Rr]= calc_inductance_Reid(L, dw, d1d, d2d,
D2r, D3r, D, M, Nd, Nr, freq, ro)
%%

rr=dw/2;
d1=d1d+dw; %m, inner diameter of driver coil
a1=d1/2; %m, inner radius of driver coil
d2=d2d-dw; %m, outer diameter of driver coil
a2=d2/2; %m, outer radius of driver coil
D2=D2r+dw; %m, inner diameter of receiver coil
R2=D2/2; %inner radius of receiver coil
D3=D3r-dw; %m, outer diameter of receiver coil
R3=D3/2; %m, outer radius of receiver coil
Aw=pi*(dw/2)^2; %cross sectional area of wire


% EM properties
mu0=4*pi*10^(-7); %V*sec/A/m, magnetic permittivity of vacuum
mu_s=0.999992*mu0; %V*sec/A/m, magnetic permeability of test specimen
```

```
I=1;%A, current (NB: all inductance values independent of current, since it
    %divides out at the end

%% Resistance Calculations

%1. Primary (Driver) Coil
lwd = d1d*pi*Nd*D; %total length of wire
Rd=(ro*lwd/Aw)+5; %Driver Resistance NOTE: Added 5 to account for BNC cables

% Detector (Receiver Coil)
lwr = D2r*pi*Nr*M; %total length of wire
Rr=(ro*lwr/Aw)+5; % NOTE: Added 5 to account for BNC cables


 %%  SELF INDUCTANCES-----------------------------------------------------------
% 1. Driver coil
Z=linspace(0,L,Nd);
a=linspace(a1,a2,D);

clear flux_single_turn
for e=1:D %r-direction, driver coil
    for f=1:Nd %z-direction, driver coil
        for i=1:D %r-direction, driver coil
            for j=1:Nd %z-direction, driver coil
                k2=4*a(i)*(a(e)-rr)*((a(i)+a(e)-rr)^2+(Z(f)-Z(j))^2)^(-1);
                [K,E] = ellipke(k2);
                A=mu0*I/pi/sqrt(k2)*sqrt(a(i)/(a(e)-rr))*((1-.5*k2)*K-E);
                flux_single_turn(i,j)=2*pi*(a(e)-rr)*A;
            end
        end
        flux(e,f)=sum(sum(flux_single_turn));
    end
end
Ld=sum(sum(flux))/I; %calculated self inductance of driver

%2. Receiver coil
R=linspace(R2,R3,M); %receiver coil
ZZ=linspace(0,L,Nr); %receiver coil

clear flux_single_turn
for e=1:M %r-direction, receiver coil
    for f=1:Nr %z-direction, receiver coil
        for i=1:M %r-direction, receiver coil
            for j=1:Nr %z-direction, receiver coil
                k2=4*R(i)*(R(e)-rr)*((R(i)+(R(e)-rr))^2+(ZZ(f)-ZZ(j))^2)^(-
1);
                [K,E] = ellipke(k2);
                A=mu0*I/pi/sqrt(k2)*sqrt(R(i)/(R(e)-rr))*((1-.5*k2)*K-E);
                flux_single_turn(i,j)=2*pi*(R(e)-rr)*A;
            end
        end
        flux(e,f)=sum(sum(flux_single_turn));
    end
end
```

```
Lr=sum(sum(flux))/I; %calculated self inductance of receiver


%% MUTUAL INDUCTANCES-------------------------------------------------------
%1. Driver to receiver
clear flux_single_turn
for e=1:M %r-direction, receiver coil
    for f=1:Nr %z-direction, receiver coil
        for i=1:D %r-direction, driver coil
            for j=1:Nd %z-direction, driver coil
                k2=4*a(i)*R(e)*((a(i)+R(e))^2+(ZZ(f)-Z(j))^2)^(-1);
                [K,E] = ellipke(k2);
                A=mu0*I/pi/sqrt(k2)*sqrt(a(i)/R(e))*((1-.5*k2)*K-E);
                flux_single_turn(i,j)=2*pi*R(e)*A;
            end
        end
        flux(e,f)=sum(sum(flux_single_turn));
    end
end

M_dr=sum(sum(flux))/I;

%2. Receiver to driver
clear flux_single_turn flux
for i=1:D %r-direction, driver coil
    for j=1:Nd %z-direction, driver coil
        for e=1:M %r-direction, receiver coil
            for f=1:Nr %z-direction, receiver coil
                k2=4*R(e)*a(i)*((R(e)+a(i))^2+(Z(j)-ZZ(f))^2)^(-1);
                [K,E] = ellipke(k2);
                A=mu0*I/pi/sqrt(k2)*sqrt(R(e)/a(i))*((1-.5*k2)*K-E);
                flux_single_turn(e,f)=2*pi*a(i)*A;
            end
        end
        flux(i,j)=sum(sum(flux_single_turn));
    end
end
M_rd=sum(sum(flux))/I;


End
```

Appendix B

MATLAB Fast Fourier Transform

```
close all
clear all
clc
% This program performs a fast fourier transfor on certain sections of the
% organoid voltage trace.

load('CuWireOrgBlock_Green.mat')

%~~~~~Smooth Data to Improve Visualization~~~~~%
voltage = smooth(voltage,71,'moving');
voltage = smooth(voltage,71,'lowess');
%~~~~~~~~~~~~~~~~~~~~~~~~~~~~~~~~~~~~~~~~~~~~~~~%

%~~~~~~~~~~~~~~~Select Time Domain~~~~~~~~~~~~~~~%
TimeStart = 73;
TimeFinish = 80;
% TimeStart = 21;
% TimeFinish = 27;
%~~~~~~~~~~~~~~~~~~~~~~~~~~~~~~~~~~~~~~~~~~~~~~~%

%~~~~~~~~~~~~~~~~Select Repitition~~~~~~~~~~~~~~~%
n = 1;
%~~~~~~~~~~~~~~~~~~~~~~~~~~~~~~~~~~~~~~~~~~~~~~~%

%~~~~~~~~~~~~~~~~~Create Arrays~~~~~~~~~~~~~~~~~%
s_time = time(TimeStart*1000+1:TimeFinish*1000)-TimeStart;
s_voltage = voltage(TimeStart*1000+1:TimeFinish*1000);
dT = TimeFinish-TimeStart;
r_time = [];
r_voltage = [];
for i=1:n
 r_time = [r_time; s_time+dT*(i-1)];
 r_voltage = [r_voltage; s_voltage];
end
%~~~~~~~~~~~~~~~~~~~~~~~~~~~~~~~~~~~~~~~~~~~~~~~%

%~~~~~~~~~~~~~~~~~~FFT Analysis~~~~~~~~~~~~~~~~~%
len = length(r_time);             % # of data points
Fs = len/(r_time(len)-r_time(1)); % Sampling frequency
T = 1/Fs;                         % Sample time
L = len;                          % Length of signal
t = (0:L-1)*T;                    % Time vector
NFFT = 2^nextpow2(L);             % Next power of 2 from length of y
Y = fft(r_voltage-mean(r_voltage),NFFT)/L;
f = Fs/2*linspace(0,1,NFFT/2+1);
%~~~~~~~~~~~~~~~~~~~~~~~~~~~~~~~~~~~~~~~~~~~~~~~%

%~~~~~~~~~~~~~~~~~~~Plot FFT~~~~~~~~~~~~~~~~~~~%
```

```
figure
stem(f,2*abs(Y(1:NFFT/2+1)))
title('Single-Sided Amplitude Spectrum of y(t)')
xlabel('Frequency (Hz)','FontSize',18)
ylabel('|Y(f)|','FontSize',18)
xlim([0 15])
% ylim([0 .2])
set(gca,'FontSize',14)
%~~~~~~~~~~~~~~~~~~~~~~~~~~~~~~~~~~~~~~~~~~~~~~~~~~~~~~~~%

%~~~~~~~~~~~~~~~~~~~Plot Trace~~~~~~~~~~~~~~~~~~%
figure
xlabel('Time (sec)')
ylabel('Voltage (mV)')
% hold all
plot(r_time,r_voltage,'k','LineWidth',2)
set(gca,'FontSize',14)
 %set(gca,'XTick',[1 25 50 75 100 125])


xlabel('Time (sec)','FontSize',18)
ylabel('Voltage (mV)','FontSize',18)
%~~~~~~~~~~~~~~~~~~~~~~~~~~~~~~~~~~~~~~~~~~~~~~~~~~~~~~~~%
```

Appendix C

MATLAB Photoelectrochemical Experiments - Voltage Conversions

```
close all
clear
%% Description
% This program takes raw (.csv file) oscilloscope voltage (lock-in amplifier
output =  Vrms = Vactual/sqrt(2)) and
% converts it to actual voltage using the lock-in sensitivity and the Vrms of
a square wave.
% For the distance experiments, MATLAB 's built in cftool is used to curve
fit the data.
% For specific exeriments, the group codes are seen below.
%% Experiment Groups Codes
% DWCGP - Deionized Water - Copper Foil(4.5mm x 18mm) - Green Laser -
Polarization
% DWCRP - Deionized Water - Copper Foil (4.5mm x 18mm) - Red Laser -
Polarization
% DCW - Deionzed Water - Copper Foil (7mm x 18mm) - Green Laser - Distance
Experiments
% DWCGC - Deionized Water - Copper Foil (4.5mm x 18mm) - Green Laser - Cu as
Part of Circuit
% DWCRC - Deionized Water - Copper Foil (4.5mm x 18mm) - Red Laser - Cu as
Part of Circuit
% RCG - Ranging pH - Copper Foil (4.5mm x 18mm) - Green Laser
% BPC - Buffer Solutions - Copper Foil Acid(4mm x 18mm)/Copper Foil Base
(4mm x 18mm) - Green Laser - Cu as part of circuit
% IND - Individual Traces
set(0,'DefaultAxesFontSize',14)
%% Lock-in Amplifier conversion constants
% converts V to mV (1000)
LRk=(1000*sqrt(2))/(20*10); %Constant for converting lock-in output voltage
(V) to actual voltage outputs (mV) (sensitivity = 20mV/V)
LRK=(1000*sqrt(2))/(1*10);  %Constant for converting lock-in output voltage
to actual voltage outputs (sensitivity = 1mV/V)
s1='octob_';
s3='.csv';
dt=10;
prompt = 'Experimental Group Code?';
EG = input(prompt,'s');
if strcmp(EG,'DWCGP') == 1;
     v=csvread(strcat(s1,'9',s3),3,1).*LRk; %mV
     t=csvread(strcat(s1,'9',s3),3,0)./60; %minutes
     figure
     plot(t(1:dt:length(t)),v(1:dt:length(v)));
      set(gca,'LineWidth',2)
    xlabel('minutes','Fontsize',16)
    ylabel('mV','Fontsize',16)
elseif strcmp(EG,'DWCRP')==1;
     v=csvread(strcat(s1,'27',s3),3,1).*LRk; %mV
     t=csvread(strcat(s1,'27',s3),3,0)/60; %seconds
     figure
```

```
     plot(t(1:dt:length(t)),v(1:dt:length(v)));
    xlabel('minutes','Fontsize',16)
    ylabel('mV','Fontsize',16)
    set(gca,'LineWidth',2)
elseif strcmp(EG,'DCW') == 1;
        file=[35:39];
    for i = 1:length(file)
      file_number=int2str(file(i));
      voltage=csvread(strcat(s1,file_number,s3),3,1).*LRk; %mV
      time=csvread(strcat(s1,file_number,s3),3,0)/60; %seconds
        m(i)=mean(voltage(1:1000));
        sD(i)=std(voltage(1:1000));
    end
    position=[1 2 5 10 15];
    Vo=m./m(1);
    V=m;
    Y=log(m);
    X=position;

    figure
    errorbar(position,m,sD,'o')
    xlabel('Distance from Foil (mm)','Fontsize',16)
    ylabel('mV','Fontsize',16)

%Curve determined using cftool using position as x data and m as y data
a2=6.053;
b2=.01832;
c2=3.596;
d2=1.09;
f2=@ (x) a2*exp(-b2.*(x-X(1)));
f3=@ (x) c2*exp(-d2.*(x-X(1)));


p=[1:.1:20];
figure
plot(X,V,'bo',p,f3(p)+f2(p),'r')
set(gca,'LineWidth',2)


figure
plot(X,V,'bo',p,f2(p),'r',p,f3(p),'k')
legend('Voltage Data','Exponential 1','Exponential 2')
set(gca,'LineWidth',2)



elseif strcmp(EG,'DWCRC') == 1;
     v=csvread(strcat(s1,'31',s3),3,1).*LRk; %mV
     t=csvread(strcat(s1,'31',s3),3,0)/60; %seconds
     figure
     plot(t(1:dt:length(t)),v(1:dt:length(v)));
    xlabel('minutes','Fontsize',16)
    ylabel('mV','Fontsize',16)
set(gca,'LineWidth',2)
     v1=csvread(strcat(s1,'32',s3),3,1).*LRk; %mV
```

```
     t1=csvread(strcat(s1,'32',s3),3,0)/60; %seconds
     figure
     plot(t1(1:dt:length(t1)),v1(1:dt:length(v1)));
    xlabel('minutes','Fontsize',16)
    ylabel('mV','Fontsize',16)
  set(gca,'LineWidth',2)
elseif strcmp(EG,'DWCGC') == 1;
     v=csvread(strcat(s1,'21',s3),3,1).*LRk; %mV
     t=csvread(strcat(s1,'21',s3),3,0)/60; %seconds
     figure
     plot(t(1:dt:length(t)),v(1:dt:length(v)));
    xlabel('minutes','Fontsize',16)
    ylabel('mV')
    set(gca,'LineWidth',2)
     v1=csvread(strcat(s1,'22',s3),3,1).*LRk; %mV
     t1=csvread(strcat(s1,'22',s3),3,0)/60; %seconds
    figure
     plot(t1(1:dt:length(t1)),v1(1:dt:length(v1)));
    xlabel('minutes','Fontsize',16)
    ylabel('mV','Fontsize',16)
    set(gca,'LineWidth',2)
 elseif strcmp(EG,'RCG') == 1;
        file=[44 42 40 41 46];
    for i = 1:length(file)
      file_number=int2str(file(i));
      voltage=csvread(strcat(s1,file_number,s3),3,1).*LRK; %mV
      time=csvread(strcat(s1,file_number,s3),3,0)/60; %seconds
        m(i)=mean(voltage(1:1000));
        sD(i)=std(voltage(1:1000));
    end
    pH=[4.3 6.5  7  7.5 9.13];
    figure
    errorbar(pH,m,sD,'bo')
    xlabel('pH','Fontsize',16)
    ylabel('mV','Fontsize',16)
    set(gca,'LineWidth',2)
elseif strcmp(EG,'BPC')
    file=[48:51];
    for i = 1:length(file)
      file_number=int2str(file(i));
      voltage=csvread(strcat(s1,file_number,s3),3,1).*LRk; %mV
      time=csvread(strcat(s1,file_number,s3),3,0)/60; %seconds
        m(i)=mean(voltage(1:900));
        sD(i)=std(voltage(1:900));
    end
    position=[4 6];
    figure
    errorbar(position,m(1:2),sD(1:2),'o');
    xlabel('Laser Position','Fontsize',16)
    ylabel('mV','Fontsize',16)
    set(gca,'LineWidth',2)
    figure
    errorbar(position,m(3:4),sD(3:4),'o');
    xlabel('Laser Position','Fontsize',16)
    ylabel('mV','Fontsize',16)
set(gca,'LineWidth',2)
elseif strcmp(EG,'IND') == 1;
```

```
prompt1='File number to plot?';
file_number = input(prompt1,'s');
voltage=csvread(strcat(s1,file_number,s3),3,1).*LRk; %mV
time=csvread(strcat(s1,file_number,s3),3,0)/60; %seconds
figure
plot(time(1:dt:length(time)),voltage(1:dt:length(voltage)));
xlabel('minutes','Fontsize',16)
ylabel('mV','Fontsize',16)
set(gca,'LineWidth',2)
end
```